ADVANCING EARTH AND SPACE SCIENCE

JGR

Journal of Geophysical Research: Oceans

RESEARCH ARTICLE
10.1029/2018JC014416

Special Section:
The Southern Ocean Carbon and Climate Observations and Modeling (SOCCOM) Project: Technologies, Methods, and Early Results

Key Points:

- Chl-a fluorescence and particle backscatter show significant vertical gradients within hydrographically defined mixed layers
- Between 20% and 80% of nighttime deep Chl-a fluorescence maxima are found within the mixed layer
- Bio-optical vertical structure appears to be linked to storm-mixing events

Supporting Information:

- Supporting Information S1
- Figure S1

Correspondence to:
M. M. Carranza,
maucarranza@ucsd.edu

Citation:
Carranza, M. M., Gille, S. T., Franks, P. J., Johnson, K. S., Pinkel, R., & Girton, J. B. (2018). When mixed layers are not mixed. Storm-driven mixing and bio-optical vertical gradients in mixed layers of the Southern Ocean. *Journal of Geophysical Research: Oceans*, *123*. https://doi.org/10.1029/2018JC014416

Received 6 AUG 2018
Accepted 10 SEP 2018
Accepted article online 17 SEP 2018

When Mixed Layers Are Not Mixed. Storm-Driven Mixing and Bio-optical Vertical Gradients in Mixed Layers of the Southern Ocean

Magdalena M. Carranza[1,2], Sarah T. Gille[1], Peter J. S. Franks[1], Kenneth S. Johnson[3], Robert Pinkel[1], and James B. Girton[4]

[1]Scripps Institution of Oceanography, University of California, San Diego, La Jolla, CA, USA, [2]Now at the Climate and Global Dynamics Division, National Center for Atmospheric Research, Boulder, CO, USA, [3]Monterey Bay Aquarium Research Institute, Moss Landing, CA, USA, [4]Applied Physics Laboratory, University of Washington, Seattle, WA, USA

Abstract Mixed layers are defined to have homogeneous density, temperature, and salinity. However, bio-optical profiles may not always be fully homogenized within the mixed layer. The relative timescales of mixing and biological processes determine whether bio-optical gradients can form within a uniform density mixed layer. Vertical profiles of bio-optical measurements from biogeochemical Argo floats and elephant seal tags in the Southern Ocean are used to assess biological structure in the upper ocean. Within the hydrographically defined mixed layer, the profiles show significant vertical variance in chlorophyll-a (Chl-a) fluorescence and particle optical backscatter. Biological structure is assessed by fitting Chl-a fluorescence and particle backscatter profiles to functional forms (i.e., Gaussian, sigmoid, exponential, and their combinations). In the Southern Ocean, which characteristically has deep mixed layers, only 40% of nighttime bio-optical profiles were characterized by a sigmoid, indicating a well-mixed surface layer. Of the remaining 60% that showed structure, ~40% had a deep fluorescence maximum below 20-m depth that correlated with particle backscatter. Furthermore, a significant fraction of these deep fluorescence maxima were found within the mixed layer (20–80%, depending on mixed-layer depth definition and season). Results suggest that the timescale between mixing events that homogenize the surface layer is often longer than biological timescales of restratification. We hypothesize that periods of quiescence between synoptic storms, which we estimate to be ~3–5 days (depending on season), allow bio-optical gradients to develop within mixed layers that remain homogeneous in density.

Plain Language Summary Storms influence high-latitude oceans by stirring the upper ocean nearly continuously. This wind mixing is usually expected to homogenize properties within the upper layer of the ocean, known as the mixed layer. New water column observations from floats and elephant seal tag confirm homogenization of hydrographic properties that determine density of seawater (e.g., temperature and salinity); however, biogeochemical properties are not necessarily homogenized. Most of the time optical measurements of biological properties within the *mixed layer* show vertical structure, which is indicative of phytoplankton biomass. These vertical inhomogenities are ubiquitous throughout the Southern Ocean and may occur in all seasons, often close to the base of the mixed layer. Within the mixed layer, observations suggest that biological processes create inhomogenities faster than mixing can homogenize. We hypothesize that 3- to 5-day periods of quiescence between storm events are long enough to allow *bio-optical* structure to develop without perturbing the mixed layers' uniform density. This may imply that phytoplankton in the Southern Ocean are better adapted to the harsh environmental conditions than commonly thought.

1. Introduction

The turbulent boundary layer, the layer of the ocean that is in direct contact with atmospheric forcing and that is actively mixing, can be fundamentally different from the mixed layer, a layer of homogenized density which may be the weakly stratified remnant layer of a past turbulent event (e.g., Brainerd & Gregg, 1995; Thorpe, 1977, 2007). Although the distinction between the former (i.e., the *mixing layer*) and the latter (i.e., the *mixed layer*) might be clear to physical oceanographers, it is not universally understood. Many investigations build on an assumption that biogeochemical tracers and/or phytoplankton are thoroughly mixed within a hydrographically defined mixed layer (e.g., Iudicone et al., 2016; Sharoni et al., 2017; Xing et al., 2012; Westberry et al., 2008). However, property distributions within the mixed layer depend on both the level of turbulence as a function of depth (e.g., Huisman et al., 1999; J. Taylor, 2016; J. Taylor & Ferrari, 2011a) and the rate at which property gradients can form (e.g., Franks, 2014).

The distributions of phytoplankton in the upper ocean depend on complex spatiotemporal interactions among biological and chemical processes, such as the responses to light and nutrients that create gradients, and physical processes, such as turbulent mixing that tend to destroy them (e.g., Therriault et al., 1978). Theoretical and numerical studies have shown that the ratio of biological to physical timescales determines biological spatial heterogeneity relative to passive tracers (Abraham, 1998; Mahadevan & Campbell, 2002; 2003; Tzella & Haynes, 2007). The trade-off between the time needed for a vertical gradient of a property to form and the time needed for mixing to destroy it determines whether the property is homogeneous or gradients can exist within a hydrographic mixed layer (e.g., Franks, 2014; Lewis, Cullen, & Platt, 1984; Lewis, Horne, et al., 1984).

Light decreases exponentially with depth; turbulence stirs phytoplankton vertically, exposing them to fluctuations in ambient light (Lewis, Cullen, & Platt, 1984). To optimize their photosynthetic capacity and/or prevent damage from high light intensity, phytoplankton respond physiologically to changes in ambient light (on timescales of less than seconds to a few hours; e.g., Claustre et al., 1994; Denman, 1983; Griffith et al., 2010; Kolber et al., 1998; Post et al., 1984; Sackmann et al., 2008). The history of their exposure to light also impacts growth rates (e.g., Denman, 1983; Marra, 1978), usually apparent as changes of biomass over timescales of several days.

Vertical distributions of photoacclimative properties (e.g., Chl-a fluorescence) ultimately depend on the competing effects of turbulence, which tends to erode gradients in the mixed layer (Falkowski, 1983), and photoacclimation of phytoplankton to the light gradient (e.g., Cullen & Lewis, 1988; MacIntyre, 2008). Vertical gradients in Chl-a fluorescence may exist in a hydrographically defined mixed layer if the timescale of photoacclimation or growth is shorter than the timescale of their mixing through the mixed layer. In contrast, uniform Chl-a fluorescence will prevail if turbulent processes are fast enough that vertical mixing occurs with a timescale shorter than that of photoacclimation.

While several theoretical studies have related vertical mixing rates to the vertical distributions of photoacclimative properties (e.g., Dusenberry, 2000; Franks & Marra, 1994; Lewis, Cullen, & Platt 1984), few in situ observations have explored vertical Chl-a fluorescence and/or phytoplankton biomass gradients within a mixed layer (Chiswell, 2011; Falkowski, 1983; Platt, 1972; Ryther & Hulburt, 1960; Therriault et al., 1990). Here we assess bio-optical vertical structure relative to hydrographic structure from novel in situ sensors deployed in the Southern Ocean, and we demonstrate that hydrographically defined mixed layers often contain significant biological vertical variance and gradients.

The Southern Ocean contains mode water formation regions that are characterized by deep winter mixed layers (e.g., Dong et al., 2008; Holte et al., 2012; Sallée et al., 2006), and it is subject to strong year-round synoptic-scale atmospheric forcing (e.g., Hodges & Lee, 2011; Vera, 2003). Deep winter mixed layers result in thick remnant mixed layers that trap water left behind once the upper ocean restratifies in spring and summer (see, e.g., Cole et al., 2010). These result in layers of weakly stratified water below the seasonal mixed layer. Storm events in summer can also lead to thinner, weakly stratified remnant mixed layers below an actively mixing layer (Talley et al., 2011). The existence of weakly stratified layers within the seasonal mixed layer can have consequences for vertical distributions of phytoplankton and/or photoacclimative properties, due to variations of turbulence intensity with depth (Huisman et al., 1999; J. Taylor & Ferrari, 2011a).

Turbulence levels within a mixed layer depend on the physical mechanisms at play in the upper ocean (e.g., convective, wind-driven, wave-driven turbulence or Langmuir circulations; Franks, 2014). For example, turbulence near the surface is influenced by atmospheric forcing (i.e., buoyancy fluxes and wind stress; e.g., Chiswell, 2011; A. Taylor & Ferrari, 2011a), whereas turbulence at the base of the mixed layer can be generated by shear instabilities and internal wave breaking (e.g., Moum & Smyth, 2001). In the Southern Ocean, the interaction of wind forcing with the surface gravity-wave field can enhance Langmuir turbulence during all seasons (Belcher et al., 2012), particularly in the presence of swell from a distant storm (McWilliams et al., 2014). Mesoscale eddies and fronts, which are ubiquitous features in the Southern Ocean (e.g., Frenger et al., 2015), also provide regions with varying levels of turbulence and convergences in the flow that may lead to plankton accumulation near fronts (e.g., Franks & Walstad, 1997; Hopkinson et al., 2007; A. Taylor et al., 2012; J. Taylor & Ferrari, 2011b; Whitt, Lévy, & Taylor 2017; Whitt & Taylor 2017). On submesoscales, mixed-layer instabilities are expected to alter stratification, vertical velocities, and turbulence intensity with depth (e.g., Callies et al., 2015; D'Asaro et al., 2011; Fox-Kemper et al., 2008; 2011; J. Taylor, 2016; Thompson et al., 2016), impacting phytoplankton vertical mixing (Lévy et al., 2012). Submesoscale restratification can lead to shallower mixing layer depths (Mahadevan et al., 2012) or reduced turbulence intensity within the mixed layer (J. Taylor, 2016) that can impact phytoplankton spring bloom initiation. The interaction of wind forcing with submesoscale horizontal buoyancy gradients may also play a role (Mahadevan et al., 2010) and can restratify or destratify the mixed layer near fronts depending on wind orientation relative to the geostrophic jet (Franks & Walstad, 1997). We thus expect significant vertical variability, in analogy with the small-scale horizontal variations of biogeochemical fields that result from upwelling and/subduction at fronts (Mahadevan & Campbell, 2002). Variability and stratification of phytoplankton (i.e., vertical gradients) within mixed layers are thus likely to occur in deep remnant mixed layers (e.g., Dusenberry & Olson, 1999); in places where turbulence may be reduced relative to a more actively mixing surface layer; in shallow, weakly stratified mixed layers that develop in the spring (e.g., Chiswell, 2011); as well as near fronts (e.g., Erickson et al., 2016; Powell & Ohman, 2015).

Due to the passage of synoptic storms, distinctive mixed and mixing layers are expected, particularly in the presence of mesoscale oceanic features (Whitt & Taylor, 2017), and have been observed in the Southern Ocean (Cisewski et al., 2005; Forryan et al., 2015). We hypothesize that intermittent atmospheric forcing from synoptic storms (with fluctuations from 2 to 10 days) may provide periods of weak turbulence long enough to allow bio-optical structures to form within a well-mixed hydrographic mixed layer (Franks, 2014). The presence of bio-optical structure within mixed layers suggests that the timescale between storm-mixing events is longer than biological timescales of restratification. The impact of a storm could come from either wind-induced mixing or storm-related buoyancy forcing that results in convective mixing of the upper ocean. Here we use storm-mixing timescales based on wind forcing as a proxy for synoptic weather events that can induce active mixing in the upper ocean.

Bio-optical in situ sensors on profiling floats and elephant seal tags that carry new biologging devices have been deployed in the Southern Ocean since 2007 (Guinet et al., 2013; Johnson et al., 2017; Russell et al., 2014), providing unprecedented bio-optical measurements that allow assessment of the vertical structure of Chl-a fluorescence and particle optical backscatter in all seasons and under sea ice (Figure 1a). Time series of Chl-a fluorescence profiles from these (Figures 1b and 1c) reveal two consistent patterns: enhancement within the mixed layer throughout all seasons (i.e., above background levels found in deep waters) and the existence of gradients and significant variance within hydrographically defined mixed layers.

Here we exploit these new measurements from floats and southern elephant seals to assess the structure of bio-optical properties and variance within mixed layers. We quantify variability in the mixed layer using variance-based metrics and assess the occurrence of structure and subsurface maxima by fitting measured profiles with typical functional forms. We present the data sets (section 2) and discuss some of their limitations (section 3). In section 3, we explain the fitting procedure and density-based mixed-layer depth (MLD) definitions. Results are presented in section 4. We provide a statistical description of the observed patterns in the Southern Ocean as a whole, though regional differences may be expected within the Southern Ocean (e.g., International Ocean – Colour Coordinating Group (IOCCG), 2015). Section 5 uses these results and satellite wind data to evaluate the relative magnitude of biological timescales of restratification versus storm-mixing timescales, and section 6 summarizes the findings.

2. Data

2.1. Southern Elephant Seal Tags

Southern elephant seals equipped with Conductivity-Temperature-Depth (CTD) satellite-relayed data loggers at sub-Antarctic islands have substantially increased the number of observations during winter and in the sea ice zone (e.g., Charrassin et al., 2008; Fedak, 2013; Roquet et al., 2013). The CTD profiles from these sensors have accuracies close to those of Argo profiling floats (Fedak, 2013; Roquet et al., 2011). CTD-satellite-relayed data logger tags deployed in the Kerguelen Islands (see Figure 1a) included a compact fluorometer (Cyclops-7 from Turner Designs) from which Chl-a fluorescence profiles can be derived (Guinet et al., 2013). These bio-logging devices were deployed on 27 elephant seals between December 2007 and February 2011. Calibration procedures included predeployment tests against High-Performance-Liquid-Chromatography (HPLC) analysis of

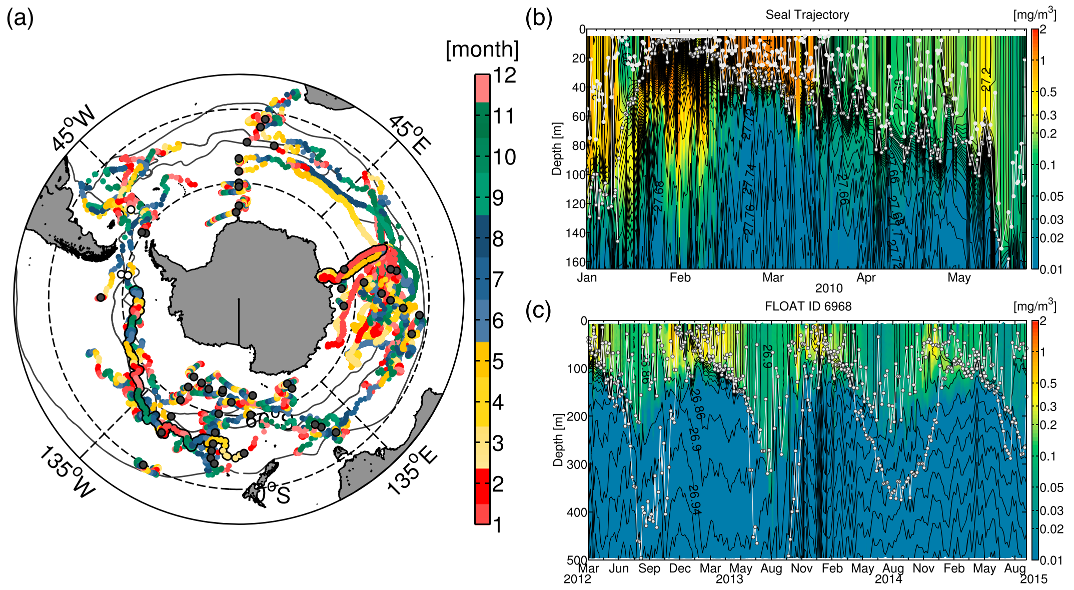

Figure 1. (a) Locations of Chl-a profiles from elephant seal tags deployed off Kerguelen Island, Electromagnetic Autonomous Profiling Explorer (EM-APEX, black circles with white fill) and Argo floats (black circles with gray fill) with bio-optical sensors, color coded by month of the year when data were collected. The mean positions of the Subtropical Front, Sub-Antarctic Front, and Polar Front from Orsi et al. (1995) are shown in black contours for reference. Chl-a as a function of time and depth, with density contours overlaid (in black), mixed-layer depth estimates using the density threshold criterion of 0.005 and 0.125 kg/m^3 (white lines) for (b) an elephant seal summer through fall round-trip from Kerguelen Island to Antarctica, and (c) an Argo float deployed in the south Pacific sector of the Southern Ocean (FloatViz ID 6968). The seal and float trajectories are indicated with black circles in (a).

filtered samples and postdeployment intercalibration of the different fluorometers (Guinet et al., 2013). During their long foraging trips, elephant seals can dive about 60 times a day, during day and night, reaching depths of up to 1,800 m (Biuw et al., 2007; Charrassin et al., 2008). Due to limitations in battery power and in the bandwidth of the Advanced Research and Global Observation Satellite system, one to three Chl-a fluorescence profiles per day were recorded in the top 180 m of the ascent (with 2-s temporal resolution) and were averaged over 10-m bins from 5 to 175 m (Jaud et al., 2012; Xing et al., 2012). The seals typically travel horizontal distances of 35–65 km per day, resulting in a spatial resolution along their track of about 25 km (Charrassin et al., 2008), covering a vast sector of the Southern Indian Ocean (Figure 1a) as they migrate to the Kerguelen Plateau, Antarctic waters, and the interfrontal zone between the Subtropical and Polar Fronts where they forage (Dragon et al., 2010). To document the prebreeding winter foraging trips, instruments were deployed in January and February at the end of the annual molt (Charrassin et al., 2010). From a total of 3,333 profiles, 1,208 profiles were acquired in fall (March-April-May), 386 in winter (June-July-August), 605 in spring (September-October-November), and 1,134 in summer (December-January-February). Observations in austral spring were less frequent than in summer, because this is the time of year when elephant seals come ashore to breed and molt (Fedak, 2013).

2.2. Biogeochemical Floats

Compared with seals, profiling biogeochemical floats provide higher vertical resolution (i.e., 2.5–5 m in the top 100 m) but coarser temporal sampling (i.e., ~5–10 days, with a few exceptions). Some of the floats deployed as part of the Southern Ocean Carbon and Climate Observations and Modeling (SOCCOM) project have ice avoidance capabilities that have allowed them to operate in regions that experience seasonal sea ice. Under sea ice or in rough sea states floats do not acquire GPS fixes at the surface; for the purposes of this study, we estimated the float position by linear interpolation of the latitude and longitude coordinates along the float trajectory. The bio-optical sensors on these floats measure Chl-a fluorescence (λ_{ex} = 470 nm, λ_{em} = 695 nm) and optical backscatter (λ = 700 nm) from which estimates of Chl-a and particle concentrations can be derived.

We use data from 51 biogeochemical Argo floats with bio-optical sensors from SOCCOM (Figure 1a, black circles with gray fill). This analysis is based on quality-controlled data from the low-resolution files (this issue; Johnson et al., 2017), last updated on 28 February 2017 and available from the SOCCOM web site (http://soccom.princeton.edu). These floats carry an Environmental Characterization Optics Fluorometer-Backscattering (ECO FLbb-AP2) or the MCOMS sensor from WETLabs, both of which have similar characteristics except for the angle of scattering in the back direction (Boss & Haentjens, 2016). They acquired over 3,700 Chl-a fluorescence and backscatter profiles, along with temperature, conductivity (salinity), and pressure, with depth-dependent vertical resolution (i.e., 5 m in the top 100 m, 10 m from 100 to 400 m, and 50 m below 400 m), typically recording 59 or 60 depth intervals during each ascending profile (depending on fluctuations in float ascent velocities) every 5 – 10 days.

Four Electromagnetic Autonomous Profiling Explorer (EM-APEX; Sanford et al., 2005) floats that also carried ECO FLbb-AP2 sensors with identical characteristics and CTDs were deployed during the Diapycnal and Isopycnal Mixing Experiment in the Southern Ocean (DIMES; Kilbourne & Girton, 2015; Ledwell et al., 2011; float IDs 4594, 4595, 4596, and 4597), providing additional Chl-a fluorescence profiles over Drake Passage and the southwest Atlantic (Figure 1a, black circles with white fill). These floats typically recorded measurements every ~2.5 m both during ascent and descent, to depths of up to ~200 m (with some exceptions), and with variable sampling intervals during their missions (from seven bursts a day to every 10 days). Due to the odd sampling behavior of some of the floats (e.g., sometimes not reaching the surface), we only use profiles that returned data in the top 10 m and that were sampled during ascent (i.e., 746 profiles), when pressure was monotonically decreasing.

Float data are distributed fairly evenly throughout the seasons (i.e., 26% in fall, 25% each in summer and winter, and 24% in spring). EM-APEX floats had a higher sampling rate just after their initial deployment, resulting in slightly more profiles in fall.

2.3. Satellite Winds

To assess storm-mixing timescales, we use Cross-Calibrated Multi-Platform (CCMP, version 2) winds, available from Remote Sensing Systems. We use 10 years of vector winds for the period June 2007 to May 2016, coincident with the floats' and seals' sampling periods. CCMP vector winds are output from a 4-D variational analysis that merges satellite winds from several wind sensors (Atlas et al., 2011). They are available at $0.25° \times 0.25°$ horizontal resolution; wind fields every 6 h represent synoptic winds. We use daily averages of the 6-hr synoptic winds to compute storm-mixing timescales reported in Table 1. We estimate the recurrence interval of storms, storm duration, and duration of periods of quiescence between storms (i.e., interstorm period), defining a high-wind event to have wind speeds exceeding 10 m/s, equivalent to force 5 on the Beaufort scale. We test the sensitivity of our results to a variable wind speed threshold, considering the duration of positive and negative wind anomalies subtracting monthly mean wind speeds at each location. (Due to gustiness in the wind, 6-hr winds give shorter storm timescales than daily-averaged winds, but the relative ratios of storm duration to interstorm time remain unchanged.)

3. Methods

3.1. MLD

Estimates of MLD are based on potential density referenced to the surface. Potential density was computed from in situ temperature and salinity profiles using the international thermodynamic equation of seawater (TEOS-10) and the MATLAB Gibbs Seawater Oceanographic Toolbox from McDougall and Barker (2011). The floats employ a Sea-Bird SBE-41 CTD, which is expected to resolve differences in density of 0.002 kg/m^3 (Kilbourne & Girton, 2015). We use standard MLD definitions from Holte & Talley's (2009) algorithm, threshold (i.e., density difference from the surface), and density gradient criteria, as well as several other thresholds. In all cases we use a surface reference depth of 10 m that avoids capturing effects of diurnal restratification (de Boyer et al., 2004).

The MLD computed from individual profiles using relatively large density difference thresholds (0.03 – 0.125 kg/m^3) represents the depth over which physical properties have been mixed in the recent past (i.e., within the last days to months). However, it does not give information on the depth range of active mixing at the time and location where the profile is acquired. The MLD, defined as the depth where density is 0.03 kg/m^3 greater than the surface, depicts the seasonal mixed layer and better captures the first spring restratification than the larger criterion of 0.125 kg/m^3 (de Boyer et al., 2004), which usually gives very deep MLDs. Unless otherwise stated, we show results for the most commonly used density threshold criterion for the Southern Ocean (i.e., 0.03 kg/m^3; de Boyer et al., 2004).

Table 1
High-Wind Event Statistics From a 10-Year Record of Daily-Averaged CCMP Winds (2007–2016)

Profile	Year-round	Winter (JJA)	Summer (DJF)
$\tau_{recurrence}$ (days)	6.73 ± 0.37	5.87 ± 0.46	7.94 ± 0.61
τ_{storm} (days)	3 ± 0.37	3 ± 0.46	2 ± 0.61
$\tau_{interstorm}$ (days)	4 ± 0.37	3 ± 0.46	5 ± 0.61
% time in storm conditions	44.59 ± 6.00	51.11 ± 8.76	25.18 ± 7.98
% sigmoid profiles	42.7 ± 1.0	48.9 ± 1.9	28.8 ± 1.9
% time in interstorm conditions	59.46 ± 6.37	51.11 ± 8.76	62.95 ± 9.15
% nonsigmoid profiles	57.3 ± 0.9	51.1 ± 1.9	71.2 ± 2.1
% homogeneous profiles (within MLD)	47.8 ± 1.0	43.5 ± 2.0	50.2 ± 2.3
% heterogeneous profiles (within MLD)	52.2 ± 1.0	56.5 ± 2.0	49.8 ± 2.3
τ_{bio} (days)	<1.5	<1	<3

Note. Storm recurrence interval ($\tau_{recurrence}$), duration (τ_{storm}), and interstorm period ($\tau_{interstorm}$) are medians (in days) of maps analogous to those shown in Figure 7. At each location, uncertainties were estimated as one standard deviation from 100 bootstrap samples of storm, interstorm, and storm cycle duration, and the median uncertainty for each map is reported in the table. For percentages of time in storm and interstorm conditions, the error is estimated by propagating the error of the ratio. Upper bounds for the biological timescale of restratification, τ_{bio}, are estimated from equations (1) and (2), using median values for τ_{storm}, $\tau_{interstorm}$, and $\tau_{recurrence}$ derived from wind speeds, an approximate fraction for homogeneous/heterogeneous profiles within the mixed layer of 0.5 and assuming $\tau_{mix} < 1$ day (based on Brody & Lozier, 2014's, 2014, study). CCMP = cross-calibrated multi-platform; JJA = June-July-August; DJF = December-January-February.

The MLD detection algorithm from Holte and Talley (2009) is designed to better capture the base of the homogeneous layer in weakly stratified regions, and it often yields shallower MLDs than the threshold criterion of 0.03 kg/m^3. (The correlation between the two MLD definitions yields $r = 0.82$, $p < 0.01$, for both float and elephant seal data.) The fine-density threshold criteria (0.01 kg/m^3 and 0.005 kg/m^3) often capture the actively mixing layer based on comparisons with microstructure data (Brainerd & Gregg, 1995). In a recent assessment of mixing layer depth, using a larger set of EM-APEX floats deployed during DIMES cruises, Kilbourne and Girton (2015) found a density threshold criterion of 0.005 kg/m^3 to be more representative of the actively mixing layer in the Southern Ocean, based on contemporaneous wind speeds.

3.2. Processing of Bio-Optical Measurements

WETLabs' calibrations of Chl-a fluorescence rely on pure Chl-a or on phytoplankton monocultures that may not be representative of in situ phytoplankton communities (Proctor & Roesler, 2010; Roesler et al., 2017). Species composition, relative pigment composition, cell size, nutrient status, growth phase, photoacclimation, and incident irradiance may all affect the relationship between fluorescence and Chl-a (Cullen, 1982; Mitchell & Kiefer, 1988; Proctor & Roesler, 2010). Although Southern Ocean waters are not considered optically complex, different phytoplankton assemblages can contain varying amounts of other pigments (e.g., Chl-b and Chl-c) that can alter the bio-optical relationships (e.g., Dierssen, 2010). Moreover, Southern Ocean waters have considerable amounts of optically active substances such as colored-dissolved organic matter (Del Castillo & Miller, 2011; Siegel et al., 2002) that may impact the retrieval of pigment fluorescence by absorbing the excitation energy. HPLC analyses of water samples are desirable to further calibrate Chl-a fluorescence at each profile, but these measurements are not possible with autonomous platforms.

Some of the float data that we use come from sensor test deployments, for which HPLC measurements from water samples at deployment sites are not available. Even if samples are collected at the deployment site (e.g., as is the case for SOCCOM floats), these are of limited utility for validating actual concentrations, because floats may sample different regimes during the course of their mission (Perry et al., 2008). There is an ongoing effort to calibrate Chl-a fluorescence using existing HPLC measurements in the Southern Ocean in combination with satellite Chl-a matchups to provide best estimates of float Chl-a concentrations (Haëntjens et al., 2017; Johnson et al., 2017). WETLabs Chl-a concentrations from floats show biases of a factor of 2–7, with WETLabs Chl-a overestimating Chl-a concentrations obtained from HPLC. Here we use WETLabs' calibration values for Chl-a concentrations divided by a factor of 2 (i.e., uncorrected Chl-a concentrations in SOCCOM quality controlled files), although detailed assessments of Southern Ocean data suggest that WETLabs Chl-a concentrations could still be biased high (e.g., Boss & Haentjens, 2016; Haëntjens et al., 2017; Roesler et al., 2017).

Because of calibration uncertainties and because we are interested in vertical gradients rather than absolute Chl-a values, in our analyses we subtract float-specific deep water (i.e., clearest water) values for each profile, which aims to correct for the contribution of nonalgal matter to the fluorescence signal that can occur at depth (see, e.g., Johnson et al., 2017; Xing et al., 2016), and we show Chl-a fluorescence profiles in relative units (i.e., rescaled by subtracting deep water values). This allows us to compare measurements from different sensors and to assess vertical structure throughout the seasons and under sea ice in a historically undersampled region.

During daylight hours and especially near noon, Chl-a fluorescence is known to be decreased by nonphotochemical quenching (NPQ, i.e., the reduction of the fluorescence emission in surface waters due to ambient irradiance), which may create deep Chl-a fluorescence maxima (Jaud et al., 2012) during the day by reducing surface fluorescence. Daytime fluorescence quenching is a recognized phenomenon in the Southern Ocean (Holm-Hansen et al., 2000) and was detected throughout the elephant seal and float data sets (Biermann et al., 2015; Boss & Haentjens, 2016; Sackmann et al., 2008; Xing et al., 2012). Although these studies have proposed methods to correct for NPQ effects, methods that would be applicable for the available float data (with the exception of one proposed by Biermann et al., 2015) rely on the assumption that fluorescence is well mixed in a hydrographic mixed layer (Sackmann et al., 2008; Xing et al., 2012). Because we wish to test this assumption, we do not correct for NPQ effects. Instead, we assess the degree of NPQ by comparing day and night Chl-a fluorescence profiles (in relative units).

We identify daytime and nighttime profiles using the local time of day at each profile location, as well as local sunrise and sunset times calculated using MATLAB functions from the AIR-SEA Toolbox (version 2.0) that were adapted by Rich Pawlowicz. Nearly 52% of the Argo profiles, 53% of EM-APEX, and 48% of elephant seal profiles were acquired during the night (i.e., 3,024 profiles). Some profiles were sampled south of the Antarctic Circle (i.e., 476 float profiles and 50 seal profiles south of 66.6°S) in areas of continuous day or night. NPQ effects could potentially last longer particularly in the high latitudes during periods with short nights near the summer solstice (Sackmann et al., 2008). However, for the bulk of the observations, the length of day ranged from 8 to 18 h. Because NPQ effects may persist for a few hours after sunset (Grenier et al., 2015; Sackmann et al., 2008; Swart et al., 2015), we tested for NPQ residual effects in nighttime profiles. We also evaluated the sensitivity of our results by adjusting the daytime/nighttime transition by $\pm$ 1 hr from sunrise and sunset times (i.e., defining daytime to be longer by including dusk and dawn profiles). Using a longer period for daytime resulted in no statistically significant differences in the percentage of nighttime profiles with DFM.

Depth-dependent changes in light can lead to changes in phytoplankton intracellular pigment concentration due to photoacclimation (see, e.g., Cullen, 1982, 2015), and a subsurface Chl-a fluorescence maximum may not correspond to a phytoplankton biomass increase. Optical backscatter (Bb), a proxy for particle concentration, provides an index that covaries with phytoplankton biomass (Behrenfeld et al., 2005; Martinez-Vicente et al., 2013) but is not susceptible to photoacclimation (Behrenfeld & Boss, 2003). For the float data for which Bb measurements are available, we have carried out our full suite of float analyses using both optical backscatter and Chl-a fluorescence.

We report optical backscatter of particles as the particle backscatter coefficient, b_{bp}. The backscatter sensor provides the volume backscatter function of both seawater and particles, $\beta(\phi, 700)$, at an angle of $\phi = 140°$ for FLbb sensors and $\phi = 150°$ for MCOMS sensors (Boss & Haentjens, 2016). Quality-controlled SOCCOM float data report b_{bp}. We compute the particle backscatter coefficient for EM-APEX float data following the same procedure. We subtract the contribution from seawater (Boss & Pegau, 2001; Sullivan & Twardowski, 2009): $b_{bp} = 2\pi\chi(\phi)(\beta(\phi, 700) - \beta_{sw}(\phi, 700))$ and use a scale factor $\chi(140°) = 1.18$ taken from Boss and Pegau (2001). Values of $\beta_{sw}(140°,700)$ are a function of temperature and salinity and are derived from the study of Zhang et al. (2009).

Before attempting to assess variance within the mixed layer or fitting profiles, we smoothed all bio-optical profiles by applying a 3-point median filter for Chl-a and a 5-point median filter for b_{bp} in order to suppress single-point maxima that could be associated with random noise. For floats, with a vertical resolution of 2.5–5 m, the median filter acts over scales of 7.5–15 m for Chl-a and 12.5–25 m for b_{pb}; for seal data with 10-m vertical resolution, the median filter has a scale of 30 m for Chl-a. Briggs et al. (2011) proposed higher-order filters, but we found that for our data, higher-order filters significantly truncated the magnitude of the subsurface maxima: the median filter is appropriate for suppressing maxima represented by a single point.

3.3. Unevenness Indices

The degree of variance of Chl-a fluorescence within the mixed layer is assessed by means of a standard deviation index (SDI), calculated as the standard deviation within the mixed layer for a given profile, normalized by the standard deviation of all measurements within the mixed layer for all observations in the Southern Ocean binned together. This normalization allows comparison of measurements from different locations and seasons. The normalization by the total mixed-layer standard deviation (i.e., for the entire Southern Ocean) facilitates comparisons with variance in hydrographic properties, which by definition should be homogeneous within the mixed layer. Small values of the SDI indicate a relatively homogeneous profile. A value close to 1 indicates that variability within the mixed layer can be as large as the variability in the entire region, and values greater than 1 indicate that variability within the mixed layer is larger than the total mixed-layer variability and thus imply a relatively heterogeneous mixed layer. By definition the mixed layer is homogeneous in density, and thus, the SDI for potential density is 2–3 orders of magnitude smaller than for Chl-a or particle backscatter, indicating that the mixed layer definitions identify layers that are homogeneous in density. The potential density SDI does not exhibit significant seasonal variability relative to bio-optical properties (not shown).

A more commonly used metric for variance in Chl-a and ecological data is the coefficient of variation, which normalizes the standard deviation by the mean (e.g., Djavidnia et al., 2010; Håkanson et al., 2003). However, the coefficient of variation is only meaningful for variables on a ratio scale (i.e., with a well-defined zero). Also, because the coefficient of variation uses the mean, it will be sensitive to Chl-a fluorescence absolute values, which are subject to large uncertainties (see section 2.2). Therefore, we have opted not to use this metric. Other metrics tested, such as the ratio between maxima and minima (i.e., $\frac{\mathrm{Chla}_{\mathrm{min}}}{\mathrm{Chla}_{\mathrm{max}}}$, as in Falkowski, 1983) were in agreement with the results presented here.

Because Chl-a fluorescence is known to be lognormally distributed (Campbell, 1995), we tested a SDI computed from log-transformed data (see, e.g., Campbell & O'Reilly, 2006). Accounting for lognormality gives higher values of the SDI particularly for the largest MLD threshold criteria, which gives deeper MLD and therefore a greater range of fluorescence, but with the same overall seasonal trends.

As another index of inhomogeneities in Chl-a fluorescence and particle backscatter in the mixed layer, we also calculate mean vertical gradients within the mixed layer, which we normalize by the mean concentration for the mixed layer.

3.4. Profile Fits and Deep Chl-a Maxima

Upper ocean Chl-a fluorescence profiles exhibit well-defined structure, sometimes with local subsurface maxima that can be smaller in magnitude than the surface value but that clearly exceed instrument noise. If we tried to identify DFM using a criterion based on a percentage increase relative to the surface (e.g., Grenier et al., 2015), we would potentially underestimate their occurrence, missing the local maxima. Instead, here we identify profiles with DFM by fitting the observed Chl-a fluorescence profiles to functional forms expected to represent a wide range of regimes, as depicted in Figure 2: (a) a sigmoid profile characterized by a well-mixed homogeneous layer, (b) a surface-intensified exponential, (c) a Gaussian representing a Chl-a maximum, (d) the combination of a Gaussian with a sigmoid, and (e) the combination of a Gaussian with an exponential. Equations for all the different functional forms largely follow the ones used by Mignot et al. (2011), and they are presented in the appendix. First guesses for fitted parameters were estimated from the observed profiles (see appendix). In particular, the depth of the Chl-a maximum was chosen based on the most prominent subsurface Chl-a fluorescence maximum (i.e., the greatest peak relative to the largest neighboring minima) if greater than the instrument noise level (i.e., 0.02 mg/m^3); otherwise, the depth of the largest peak (i.e., the absolute maximum) was chosen. The most prominent subsurface peak was usually deeper than the largest peak, which is based on Chl-a fluorescence absolute values (i.e., irrespective of neighboring values), which generally increase toward the surface. The depth of the most prominent peak (as opposed to the depth of the largest peak) was preferred to avoid attempting to fit Gaussians to less prominent maxima close to the surface and failing to fit Gaussians to more prominent peaks below the surface mixed layer.

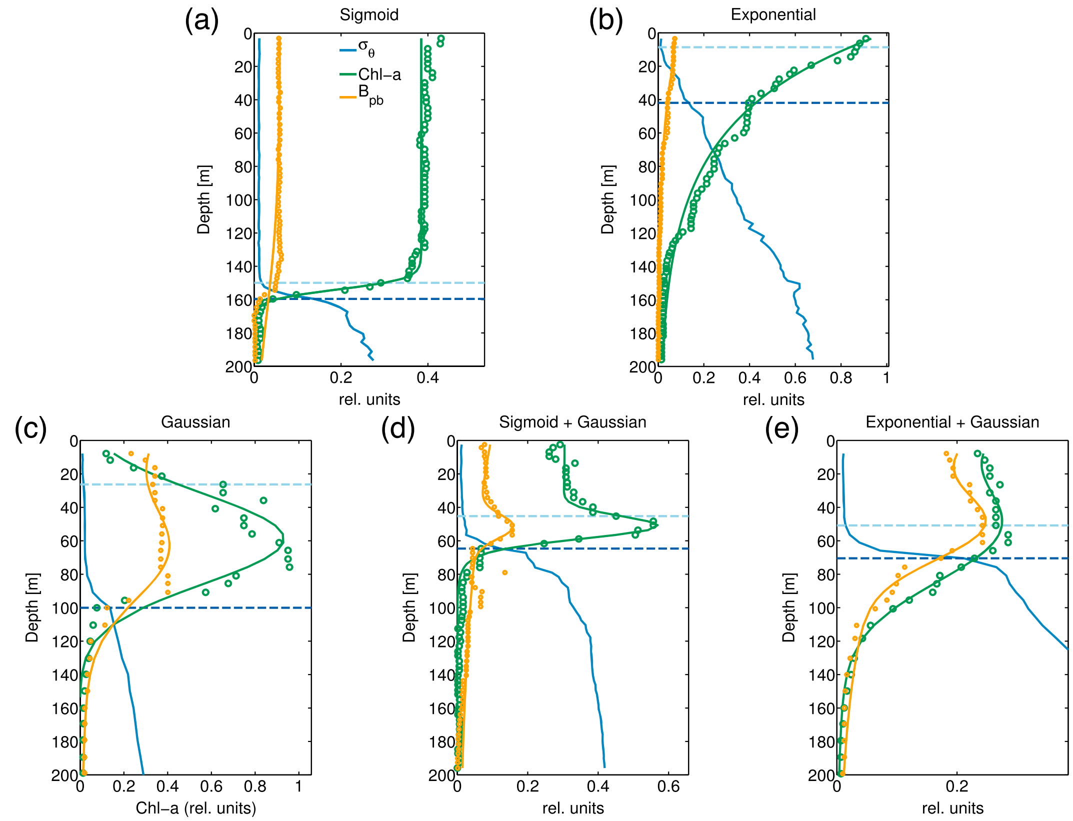

Figure 2. Examples of nighttime Chl-a fluorescence (green) vertical profiles fitted to a (a) sigmoid, (b) exponential, (c) Gaussian, (d) Gaussian + sigmoid, and (e) Gaussian + exponential. Sigmoid profiles are consistent with a homogeneous profile near the surface, while Gaussian profiles have a subsurface maximum. The best fit (line) to the observations (circles) was selected based on a Chi-square goodness of fit test with constant standard deviation of twice the instrument noise level (i.e., 0.04 mg/m^3) and taking into account the number of fitted coefficients (see appendix). Particle backscatter profiles and fits (yellow) and density profiles (blue) are also shown, along with the deepest and shallowest estimates of mixed-layer depth (dashed lines). All profiles are shown in relative units, rescaled by subtracting the surface value for σ_θ and deep water values for Chl-a and b_{pb}, and multiplying b_{pb} by 100.

The best fit model for each profile was chosen based on a 95% confidence Chi-square test for goodness of fit (e.g., Press et al., 2007), which takes into account the number of fitted parameters for each functional form. That is, for each fitted fluorescence profile we computed $\chi^2 = \sum_{k=1}^{N}(F_k - \mu_k)^2/s^2$, where N is the number of observations in each profile, F_k is the observed, and μ_k the modeled fluorescence value at each depth level, assuming a constant standard deviation of $s = 0.04$ mg/m^3 (i.e., twice the instrument noise level in deep water to be more conservative). Large values of the sample Chi-square indicate significant deviations from the modeled values. To avoid overfitting, only profiles with at least 17 observations (i.e., the maximum possible number of observations for elephant seal profiles) were fit. The smallest profile Chi-square (i.e., among all functional forms tested) was compared to the critical Chi-square value (i.e., for a 5% significance level) from a theoretical Chi-square distribution with $\nu = N - m$ degrees of freedom, where m is the number of fitted parameters in the model (see appendix). If the profile Chi-square was smaller than the critical Chi-square, then the fitted profile was chosen as the best model fit; otherwise, it was rejected.

We took a conservative approach in defining profiles with DFM. In total 60% of all nighttime Chl-a fluorescence profiles were Gaussian (i.e., (c), (d), or (e)), and most Gaussians were embedded in a homogeneous layer (i.e., 58% were best represented by (c), and the remainder approximately evenly split between (d) and (e)). Approximately 13% of the Gaussian fits showed maxima located near the surface (i.e., $\leq$ 20-m depth) and were not considered in our analyses of DFM. Gaussian fits with subsurface maxima (47% of the total) were interpreted as having a DFM only if peak prominence was greater than 0.04 mg/m^3. In addition, all profile fits were visually inspected for consistency, and in a few cases in which the subsurface maximum was larger in the fit than in the observations, the profile was reevaluated based on the smallest Chi-square. In total ~ 37% of all nighttime

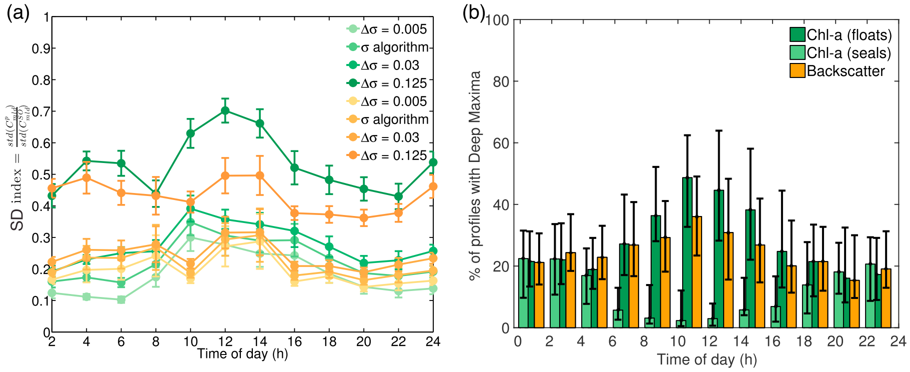

Figure 3. (a) Diurnal standard deviation index (SDI) within the mixed layer (i.e., the standard deviation within the mixed layer normalized by the total standard deviation for all Southern Ocean's mixed-layer observations in each time interval) for Chl-a fluorescence (green) and particle backscatter (yellow). Color shades indicate different mixed-layer depth (MLD) definitions (see legend), and error bars represent the standard error of the mean for each time interval. (b) Percentage of mixed layers with deep maxima for Chl-a fluorescence from seals (light green) and floats (dark green), and particle backscatter (yellow), using the most commonly used density threshold of $\Delta\sigma = 0.03$ mg/m^3 to define MLD. Error bars in (b) indicate the sensitivity to the MLD definition used: $\Delta\sigma = 0.125$ mg/m^3 (upper bound) and $\Delta\sigma = 0.005$ mg/m^3 (lower bound). Note that seal data were corrected for non-photochemical quenching (NPQ) effects (Guinet et al., 2013), suppressing deep fluorescence maxima within the mixed layer.

Chl-a fluorescence profiles were identified as having a DFM. For all profiles with DFM (i.e., deeper than 20 m), DFM magnitude and DFM depth were well correlated with those inferred from the profile fits ($r = 0.96$ for DFM magnitude and $r = 0.92$ for DFM depth, for $N = 1251$, and 99% confidence).

In addition, for float profiles with concomitant backscatter measurements, we fit smoothed b_{pb} profiles to the same functional forms. We tested for the existence of deep backscatter maxima (DBM) using an analogous procedure, assigning the depth of the DFM as a first guess parameter for the depth of the DBM. Of all nighttime float b_{pb} profiles for which Chl-a fluorescence showed a DFM (i.e., 37 %), 75% were fit by Gaussians, with a large fraction of the remainder (i.e., 22%) not assigned a fit. Visual inspection of the latter showed subsurface features in b_{pb} that were correlated with the DFM; however, the presence of secondary peaks in b_{pb} hindered the calculation of a profile fit.

Because seal and float data have different vertical resolutions (i.e. ~2.5 m for EM-APEX, 5 m for Argo, and 10 m for seal data), we tested the sensitivity of our results by resampling all observations with a common 10-m vertical resolution. The original higher-resolution data consistently show larger percentages of DFM and DBM, but the differences are small and within error bounds.

4. Results

Despite deep mixed layers in the Southern Ocean, most bio-optical profiles show structure. Only ~40% of nighttime Chl-a fluorescence profiles were best fit by sigmoids (fully 97% of the non-Gaussian profiles were sigmoids, (a) in Figure 2a). This implies that depth variability in biological activity is sufficiently large that mixed-layer vertical stirring does not obliterate its signature.

After evaluating the use of nighttime Chl-a fluorescence as a proxy for phytoplankton biomass from diurnal changes in mixed-layer bio-optical properties (section 4.1), we assess the occurrence and prominence of DFM throughout the year (section 4.2). We then compare the depth of prominent deep fluorescence maxima (DFMD) with the MLD, for a suite of possible MLD definitions, and quantify the number of profiles with DFM that lie above the MLD for each month of the year (section 4.3). Finally, we quantify mixed-layer variability in bio-optical properties, which we contrast with mixed-layer variability in hydrographic properties (section 4.4).

4.1. Diurnal Chl-a and b_{pb} Variability in the Mixed Layer

Fluorescence can respond to changing light levels by photoacclimation, without any changes in phytoplankton biomass or hydrographic properties. To evaluate this, we first examine Chl-a fluorescence and particle backscatter within the mixed layer as a function of time of day. Within the mixed layer, the SDI for fluorescence variability peaks within ±4 hr of local noon (green lines in Figure 3a), consistent with NPQ driving significant gradients under peak light conditions. However, the percentage of deep maxima in Chl-a fluorescence agrees

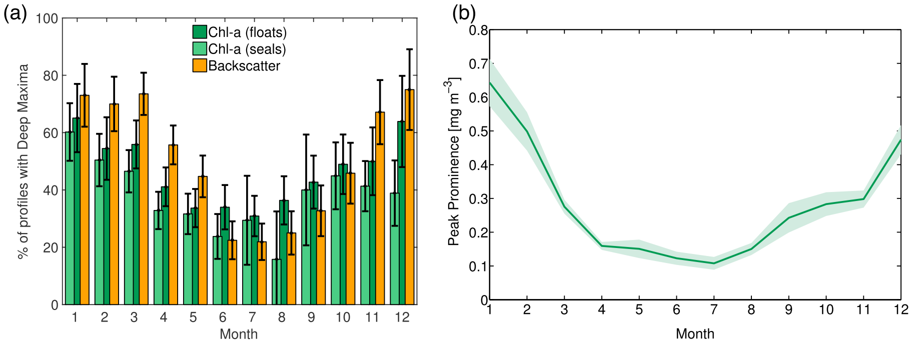

Figure 4. (a) Percentage of nighttime Chl-a fluorescence profiles with a deep fluorescence maximum (DFM) for elephant seals (light green) and floats (dark green) in each month. Here a DFM is identified as a profile best fit by a Gaussian, with a prominent peak below the surface (see section 3.4). The percentage of b_{pb} profiles fit by Gaussians is also shown (yellow). Bio-optical float data were averaged in 10-m bins to match the resolution of seal data before fitting profiles. Error bars give the 95% confidence interval estimated from a bootstrap method. (b) Seasonality of DFM peak prominence (i.e., maximum Chl-a fluorescence relative to the largest neighboring minimum). Shaded areas indicate the standard error of the monthly means.

well with deep maxima in b_{pb} (yellow lines in Figure 3a), indicating that not all diurnal variability in Chl-a fluorescence is associated with NPQ. The daytime peak in backscatter suggests that the diurnal cycle of light may stimulate phytoplankton growth, producing real changes in phytoplankton biomass and particle concentrations (e.g., Davis et al., 2008; Gardner et al., 1995; Stramska & Dickey, 1992). Phytoplankton-zooplankton interactions may also explain diurnal changes in phytoplankton biomass (e.g., Priddle et al., 1997).

Although Figure 3a indicates general agreement in Chl-a fluorescence and b_{pb} daytime peaks, as noted in section 3.2, in this study, we avoid concerns about the multitude of processes that may be active during the day by focusing on nighttime Chl-a fluorescence. Chl-a fluorescence variability agrees well with variability in particle backscatter as indicated by both the SDI as a function of local time of day (Figure 3a) and the co-occurrence of deep maxima in Chl-a and b_{pb} (Figure 3b). This suggests that variability in Chl-a fluorescence at night is likely associated with variability in phytoplankton biomass. This is in agreement with relationships between Chl-a concentrations and particle backscatter derived from satellite observations (Behrenfeld et al., 2005) and in situ Chl:Cp (beam attenuation) observations (Behrenfeld & Boss, 2006), showing that changes in Chl-a concentrations are closely related to changes in phytoplankton biomass for the Southern Ocean. In Antarctic waters, Strutton et al. (1997) also showed that high spatial variability in nighttime Chl-a fluorescence correlates with high phytoplankton productivity, as inferred from high-resolution transects of photosynthetic parameters.

4.2. Seasonality of Deep Chl-a Fluorescence Maxima Ocurrence

The percentage of profiles with DFM and DBM is high in summer, when stratification is strong, with more than half the profiles presenting DFM and/or DBM (Figure 4). However, Figure 4 also shows that subsurface enhancement in nighttime Chl-a fluorescence is significant year-round in float and seal data, as well as in nighttime particle backscatter profiles from floats.

4.3. Deep Chl-a Fluorescence Maximum Depth and MLD

The DFM can lie above or below the MLD, depending on physical conditions and on the definition used for a mixed layer. The joint probability density function (PDF) in Figure 5a illustrates the relationship between DFMD and MLD, here using the MLD threshold criterion of 0.03 kg/m^3. The maxima in the PDF occur when MLD is slightly deeper than the DFMD, indicating that DFM are often found at the base of the mixed layer.

A significant fraction of profiles have DFM that are shallower than the MLD, even for the fine threshold criterion of 0.005 kg/m^3, which may be more closely related to the mixing layer depth. The sensitivity of the percentage of nighttime DFM that are shallower than the MLD to the criterion used to define the MLD is shown in Figure 5b, for each month of the year. Smaller density threshold criteria generally show a lower percentage of profiles with DFM above the MLD than do larger threshold criteria. In summer, 20% to 80% of DFMs are within the mixed layer, depending on the definition of MLD. In winter the spread is narrower, with all MLD definitions showing that more than 70% of DFMs are within the mixed layer.

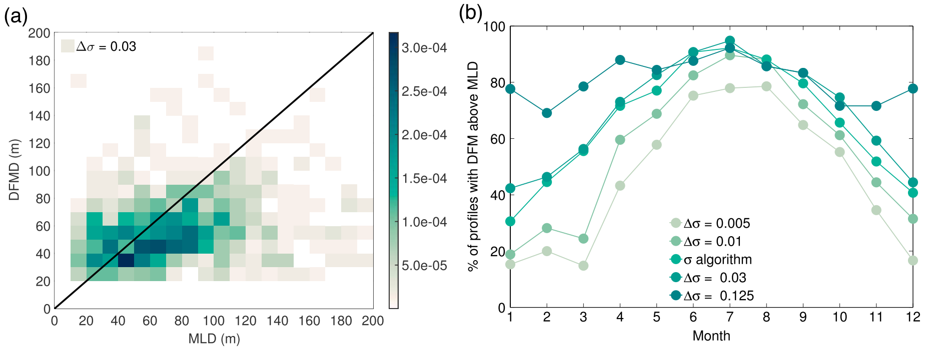

Figure 5. (a) Two-dimensional probability density function (PDF) of deep fluorescence maximum depth (DFMD) and the mixed-layer depth (MLD) using a density threshold of 0.03 kg/m^3. (b) Percentage of Chl-a fluorescence profiles with a deep fluorescence maximum (DFM) that are above the MLD (of all profiles that show DFM) for several definitions of MLD (see legend) in each month of the year. Data include only nighttime profiles from elephant seals, EM-APEX, and Argo floats characterized by having DFM deeper than 20 m with Chl-a fluorescence at the maxima at least twice as large as the fluorometer noise level (i.e., 0.04 mg/m^3).

Based on occurrences of DFM within the MLD, it might appear that the mixed layer is less homogeneous (or mixing the least) in winter than in summer. While almost all DFM in winter occur within the mixed layer (e.g., ~25% over all profiles for the finest density threshold criterion), only ~12% of all profiles show the DFM within the shallowest MLD in summer (Figures 4a and 5b). However, DFM in winter are less prominent than in summer (Figure 4b). In the next section, we present seasonality in bio-optical heterogeneity based on mixed-layer variance in bio-optical properties, which accounts for peak magnitude.

4.4. Seasonal Chl-a and b_{pb} Variability in the Mixed Layer

Nighttime DFM above the MLD indicate the existence of biological gradients within the hydrographic mixed layer. The SDI, which quantifies mixed-layer variability in a profile relative to total mixed-layer variability for the Southern Ocean, is enhanced in spring and summer for bio-optics (green and yellow lines in Figure 6); and bio-optical properties are consistently more heterogeneous than temperature (blue in Figure 6), salinity, and density (not shown) for all mixed-layer definitions (see supporting information).

The SDI for nighttime Chl-a fluorescence peaks in December and is lowest from May to August (green line in Figure 6); the SDI for b_{bp} peaks in November, during the spring bloom (yellow line in Figure 6). While the SDI index for temperature (blue line in Figure 6) is <0.05 year-round, nighttime Chl-a fluorescence and b_{pb} profiles vary by a much larger fraction of the total mixed-layer variability for all definitions used for the MLD. The monthly averaged SDI for nighttime Chl-a fluorescence in the mixed layer (green in Figure 6a) varies between ~0.1 for the fine-density threshold criterion and nearly 0.8 for the largest threshold used for a mixed layer

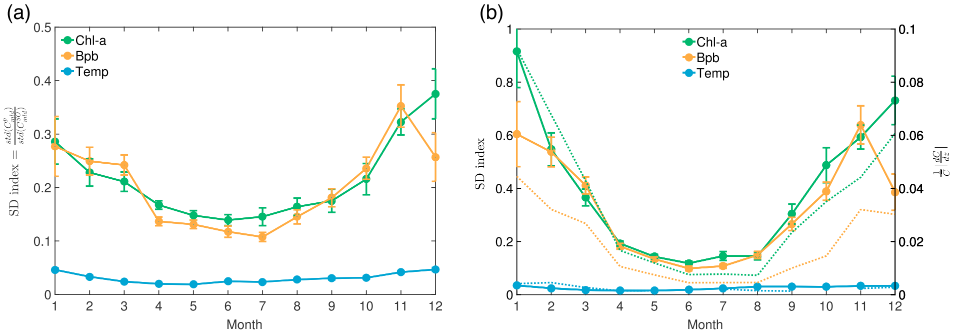

Figure 6. Monthly standard deviation index (SDI) within the mixed-layer depth (MLD) for nighttime Chl-a fluorescence (green), particle backscatter (yellow), and temperature (blue), using the 0.03 mg/m^3 threshold criterion for the MLD (see supporting information for sensitivity to MLD definition). (a) Normalizing the vertical standard deviation within the mixed layer in each profile by the total mixed-layer standard deviation across the full Southern Ocean in each month and (b) normalizing the vertical standard deviation within the mixed layer in each profile by the total wintertime mixed-layer standard deviation across the Southern Ocean (see section 3.3). Mean vertical gradients (i.e., averaging absolute values) are also shown in dashed lines (right y axis) in (b). Error bars are the standard error of the mean for each month.

(see supporting information for sensitivity to MLD definition). This shows that while temperature variability in mixed layers is small, the Chl-a variability in the mixed layer is a significant fraction of the total mixed-layer Chl-a variability in the Southern Ocean. Chl-a fluorescence variability within the mixed layer for a given day is, on average, between 15% and 40% of the total mixed-layer variability across the entire Southern Ocean.

A large range of variability is not uncommon in bio-optical data (Campbell, 1995). A second version of the SDI (Figure 6b) uses total variability in July as a normalization, thus allowing comparison of vertical variability relative to the total Southern Ocean mixed-layer variability in austral winter. July variability is expected to be the smallest due to the relatively strong activity of storms (e.g., Simmonds et al., 2003; Ulbrich et al., 2009) that presumably vertically homogenize upper-ocean properties throughout the Southern Ocean. The high frequency and large spatial scales (O(100 – 1000 km)) of storms make it more likely that any given profile will be sampled beneath an active storm and exhibit a thoroughly mixed surface layer. One might expect that bio-optical variance within the mixed layer for a given profile would be less than the total variance across all mixed-layer measurements in winter. Results depend strongly on the MLD definition chosen (see supporting information). For example, for the month of December, this version of the index varies from ∼0.4 for a fine-density threshold criterion to nearly 2.2 for the largest threshold. These numbers indicate that vertical variability in bio-optical properties within a mixed layer can be a significant fraction of wintertime mixed layer variability across the Southern Ocean.

The seasonal dependence of inhomogeneity in nighttime Chl-a fluorescence and b_{pb} profiles (Figure 6b, thick lines) shows greater variability within hydrographic mixed layers in spring and summer months, during the phytoplankton growth season. In general, Chl-a fluorescence in the mixed layer is more homogeneous in late fall and winter, consistent with the seasonal deepening of the MLD and a hydrographic mixed layer more closely related to the mixing layer (Chiswell, 2011). Departures from homogeneity relative to the winter variability (i.e., $SDI > 0.2$) occur in late winter, when sudden restratification may occur (see, e.g., Figures 1b and 1c) and the MLD is likely a poor proxy for the mixing layer depth. Vertical gradients in Chl-a fluorescence within the mixed layer show similar seasonality (Figure 6b, dashed lines). Chl-a fluorescence and b_{pb} variability within the mixed layer are also enhanced (e.g., relative to potential density) when we consider only profiles that were fit by sigmoids (not shown), suggesting differences between hydrographically and optically derived mixed layers (see, e.g., Zawada et al., 2005).

5. Discussion

5.1. Occurrence of DFM

DFM are widespread features in stratified surface waters of the global ocean (e.g., Lavigne et al., 2015; Mignot et al., 2014) and can result from a broad range of interacting processes (see, e.g., Beckmann & Hense, 2007; Gong et al., 2015; Cullen, 2015). Deep Chl-a maxima have been previously documented in pelagic waters of the Southern Ocean (Charrassin et al., 2010; Erickson et al., 2016; Gomi et al., 2010; Grenier et al., 2015; Holm-Hansen & Hewes, 2004; Holm-Hansen et al., 2005), though mostly in the summer season when the upper ocean is well stratified and a shallow seasonal mixed layer develops. Although not as persistent and prominent as DFM in oligotrophic regions (Figure 4b and see, e.g., Mignot et al., 2014) or coastal environments (e.g., Cullen & Eppley, 1981), the DFM we observed are ubiquitous throughout the Southern Ocean and can occur regardless of the season. Elephant seal data also showed that numerous areas had DFM that were undetectable by satellite remote sensing, with fluorescence intensities up to 5 times the surface values (Charrassin et al., 2010); these were also identified in nighttime profiles by Biermann et al. (2015).

Nighttime DFM in the Southern Ocean are more often found at or near the base of the mixed layer (Figure 5a), suggesting the importance of strong density gradients and/or turbulence at the base of the mixed layer for the formation and maintenance of DFM. Remarkably, a significant number of DFM are found *within* the mixed layer, regardless of the criterion chosen to define the mixed layer (Figure 5b). This is true year-round for the most commonly used definitions of MLD (e.g., de Boyer et al., 2004; Holte & Talley, 2009), including during winter and spring for the fine-density threshold criterion of Kilbourne and Girton (2015). The large range of variability in the fraction of profiles with DFM above the MLD for different MLD definitions (∼20 – 80%; Figure 5b) suggests that caution should be exercised when defining the layer that is assumed to be mixed in Chl-a fluorescence: nearly 20% of profiles with subsurface maxima have these maxima above the MLD, even when a fine-density threshold criterion for MLD detection is used. Particularly in summer, whether the DFM lies above or below the MLD is largely dependent on the MLD threshold criterion used. The fact that most

DFM lie below the MLD defined by fine-density thresholds but above MLDs defined by larger threshold criteria suggests that reduced turbulence in remnant mixed layers may allow DFM to form below the active mixing within the mixed layer.

5.2. Mixed-Layer Variance in Bio-Optical Properties

The high degree of variance we observe in mixed-layer nighttime Chl-a fluorescence and particle backscatter statistics is enhanced in the summer and not observed in hydrographic properties (Figure 6), indicating that biological processes frequently dominate vertical mixing in the mixed layer. Submesoscale features within the mixed layer have been observed in the Southern Ocean (Adams et al., 2017; Bachman et al., 2017) and can be important in shaping the local distributions of bio-optical properties and biogeochemical tracers in the Southern Ocean (du Plessis et al., 2017; Long et al., 2012; Read et al., 2007; Resplandy et al., 2014; Rosso et al., 2016), even in the summertime (Erickson et al., 2016; Viglione et al., 2018). Thus, submesoscale variability could explain some of the observed mixed-layer bio-optical variance. However, the net impact of submesoscale dynamics on larger scales is less clear (Lévy et al., 2012; Resplandy et al., 2009, 2014). Assessing the role of submesoscale dynamics and sources of variance in mixed-layer hydrographic properties is outside the scope of this paper (as it would require higher vertical resolution and measurements of the flow field that are unavailable for most profile observations). Nonetheless, the large variability that we observe in mixed-layer bio-optical properties (compared to hydrographic properties, e.g., Figure 6) suggests that, to first order, variance in bio-optical properties within mixed layers is likely linked to biological processes.

Numerous observational studies have reported spatial structure in bio-optics and phytoplankton within the mixed layer that was uncorrelated with structure in the physical environment (e.g., Currie & Roff, 2006; Denman & Gargett, 1995; Mackas et al., 1985; Strutton et al., 1997; Therriault et al., 1978), though most have looked at horizontal variability and few have analyzed vertical structure and variance within mixed layers. Comparisons of power spectra for physical and biological parameters show that the bio-physical coupling/decoupling is scale dependent and indicate that on intermediate scales (i.e., 30–400 m) typical of MLDs, phytoplankton may not behave as a passive tracer (Currie & Roff, 2006). Using coastal observations, Therriault et al. (1978) found bio-optics to be uncorrelated with temperature most of the time, implying that biological processes dominate the formation of structure in bio-optics, except when storm-driven turbulence is strong enough to overcome the creation of gradients and heterogeneity by biological or chemical processes. In the next section, we discuss vertical structure in bio-optical profile data in relation to wind-driven (or storm-related buoyancy driven) turbulence, under the assumption that the relative magnitudes of storm-mixing rates and biological processes determine the degree of heterogeneity in bio-optical vertical structure.

5.3. Biological Restratification and Storm-Mixing Timescales

Timescales of biological processes that alter Chl-a fluorescence are expected to range from seconds to a few days. Diurnal variability in mixed-layer Chl-a fluorescence (Figure 3a), as well as the percentage of profiles with DFM as a function of local time of day (Figure 3b), peaks near local noon, but decays to relatively constant nighttime values within a few hours. This suggests that photoacclimation is sufficiently fast to respond to diurnal variability (within a few hours, <6 hr). However, the DBM also shows diurnal variability, which suggests that not all diurnal Chl-a fluorescence variability within the mixed layer is due to photoacclimation, and it may instead reflect changes in biomass through growth and mortality and/or possibly by vertical migration (see e.g., Cullen, 2015; Pearre, 2003). Shipboard incubations of water samples from the Southern Ocean typically show changes in Chl-a concentrations after several days, even during Fe-addition experiments when phytoplankton growth is expected to be enhanced (>3–4 days, see, e.g., de Baar et al., 2005; Martin et al., 1990; Smetacek et al., 2012). Timescales for phytoplankton growth are difficult to quantify with the relatively sparse observations at hand. Nonetheless, to the extent that nighttime Chl-a fluorescence is indicative of phytoplankton biomass, the structure of nighttime vertical profiles can provide insights into the biological timescales of restratification relative to mixing timescales.

From all nighttime Chl-a fluorescence profiles evaluated in this study, only ~40% are homogeneous (i.e., fit by a sigmoid); nearly 60% show some degree of heterogeneity (i.e., fit by some type of Gaussian or exponential form), suggesting that vertical variability and gradients in bio-optical properties in the Southern Ocean surface layer are common. During the phytoplankton growing season (September–March), the percentage of heterogeneous profiles increases to ~75%. In Table 1, we contrast percentages of homogeneous versus heterogeneous nighttime Chl-a fluorescence profiles for winter and summer months. We hypothesize that the heterogeneous profiles form, especially in summer, because the timescale of biological processes that allow gradients in nighttime Chl-a fluorescence to form (or biological timescale of restratification, τ_{bio}) is shorter than the timescale between mixing events that homogenize the surface layer, τ_{nomix}, that is, $\tau_{\text{bio}} < \tau_{\text{nomix}}$.

Working from the hypothesis that Southern Ocean storms are one of the dominant drivers of the turbulent processes that homogenize the upper ocean (e.g., Cisewski et al., 2005; Forryan et al., 2015; Kilbourne & Girton, 2015), we can estimate τ_{nomix} as the duration of the quiescent interval between storms from satellite wind data. While the duration of a storm (i.e., τ_{storm}) is indicative of the timescale over which a heterogeneous bio-optical profile can be rehomogenized, the time interval between two successive high-wind periods or interstorm period (i.e., $\tau_{\text{interstorm}}$) will indicate whether there is sufficient time for biological processes to create gradients and is the relevant timescale for the formation of bio-optical structure. Note that in the context of our discussion, the relevant mixing timescale is different from the timescale of vertical mixing (i.e., τ_{mix}, or average time it takes a particle to mix from the surface to the bottom of the turbulent layer; e.g., Franks, 2014), which is expected to be < 1 day (see their Figure S4 ; Brody & Lozier, 2014) and is related to the time it might take a strong wind to rehomogenize a vertical gradient (i.e., a small fraction of τ_{storm}). In this context, the relevant mixing timescale is the duration of weak mixing within a storm cycle (i.e., $\tau_{\text{nomix}}=\tau_{\text{interstorm}}$), when phytoplankton can restratify.

The recurrence period of storms, $\tau_{\text{recurrence}}$, is defined as the record length (in days) divided by the number of storm events (e.g., Dorsch et al., 2008) and gives the average duration of a storm cycle (i.e., $\tau_{\text{recurrence}}=\tau_{\text{storm}} + \tau_{\text{interstorm}}$ or the time elapsed between the beginning of a storm and the beginning of the next one). $\tau_{\text{recurrence}}$, τ_{storm}, and $\tau_{\text{interstorm}}$ were computed at each location from the CCMP wind record (Figure 7), defining a storm-mixing event to have wind speeds >10 m/s (see, e.g., Hodges & Lee, 2011). $\tau_{\text{recurrence}}$ from year-round satellite observations is on average 6.9 days (Figure 7a and Table 1). Once-a-week storms are consistent with statistics derived from extratropical cyclonic activity in the Southern Hemisphere (e.g., Hodges & Lee, 2011; Simmonds & Keay, 2000). PDFs of τ_{storm} and $\tau_{\text{interstorm}}$ at each location follow exponential distributions (i.e., longer interstorm periods are less frequent) for interstorm periods longer than 2–3 days, as expected from a Poisson process (e.g., Dorsch et al., 2008; Eagleson, 1978). Maps of medians for τ_{storm} and $\tau_{\text{interstorm}}$ from year-round observations are presented in Figures 7b and 7c. Based on year-round satellite winds, the median $\tau_{\text{interstorm}}$ for the Southern Ocean is 4 days (i.e., median for map in Figure 7c), and at any given location it is consistently slightly longer than the median τ_{storm} (i.e., 3 days, Figure 7b and Table 1). τ_{storm} is in good agreement with the mean lifetime of Southern Hemisphere extratropical cyclones from 40 years of reanalyses for the period 1958–1997 (Simmonds & Keay, 2000), which was found to be slightly over 3 days (Simmonds & Keay, 2000; their Figure 9).

The durations of storms, interstorm periods, and storm cycles exhibit seasonality at any given location. In winter, storm events are slightly more frequent and last longer than in summer (Table 1). The median duration of interstorm periods is 3 days in winter versus 5 days in summer (Table 1 and Figure 7d). Although Simmonds and Keay (2000) found little seasonality in along-track duration of winter versus summer Southern Hemisphere cyclones, cyclonic systems are usually more frequent in winter than in summer. In their study, the strongest seasonality occurred in the 30–50° S latitude band, where we find $\tau_{\text{interstorm}}$ increases by 1–2 days (Figure 7b and 7c). We hypothesize that this slight increase in $\tau_{\text{interstorm}}$ may impact phytoplankton bloom development, helping to foster the development of subsurface gradients during summer months.

From these storm timescales, it is possible to constrain biological timescales of restratification in a statistical sense (see Figure 8). One might predict that when a storm starts, the upper ocean begins to mix. After a period of time, τ_{mix}, density and bio-optical profiles are fully homogenized within the mixed layer, and they will remain homogenized until the end of the storm for a time period $\tau_{\text{storm}} - \tau_{\text{mix}}$. After the storm ends, density remains homogenized, but bio-optical properties reestablish gradients over a time period τ_{bio}. Thus, the predicted fraction of homogeneous profiles over a storm cycle (i.e., $\tau_{\text{recurrence}}$) would be given by the following:

$$f_{homogeneous} \sim \frac{\tau_{\text{storm}} - \tau_{mix} + \tau_{\text{bio}}}{\tau_{\text{recurrence}}}, \tag{1}$$

where $f_{homogeneous}$ is the fraction of homogeneous profiles estimated from all fitted fluorescence profiles. In the same manner, the predicted fraction of heterogeneous profiles is expected to be given by the following:

$$f_{\text{heterogeneous}} \sim \frac{\tau_{\text{mix}} + \tau_{\text{interstorm}} - \tau_{\text{bio}}}{\tau_{\text{recurrence}}}, \tag{2}$$

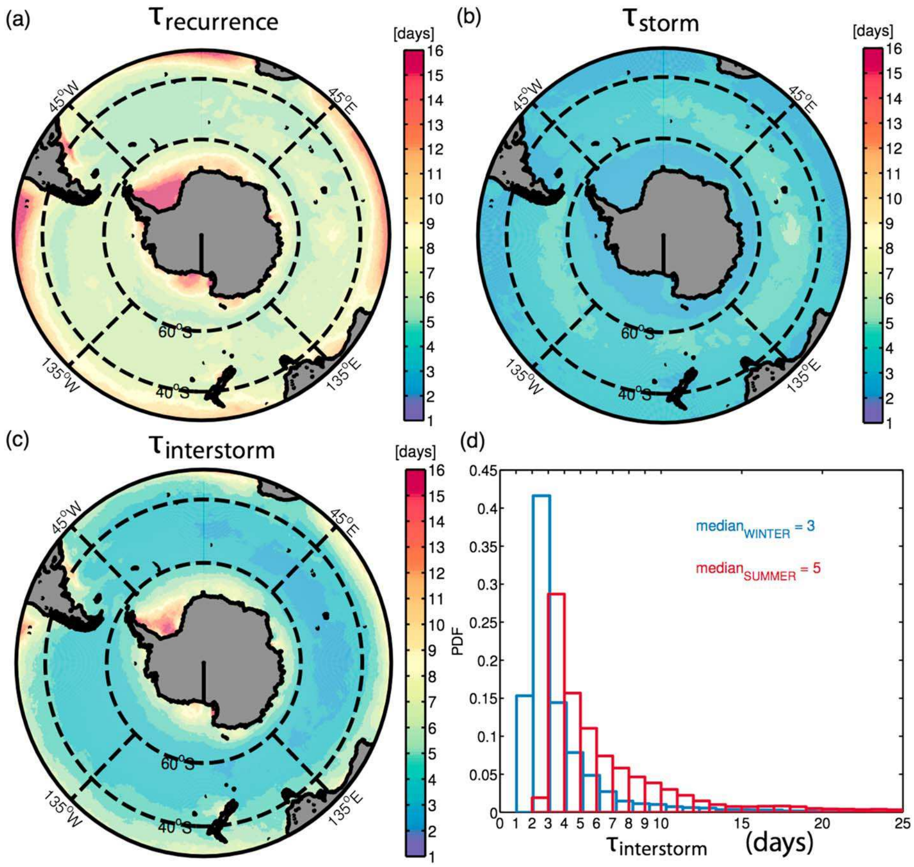

Figure 7. (a) Recurrence time interval of storms (i.e., $\tau_{\text{recurrence}}$), considering a storm as an event characterized by wind speeds greater than 10 m/s. (b) Median duration of storms (i.e., τ_{storm}). (c) Median duration of interstorm periods (i.e., $\tau_{\text{interstorm}}$). (a), (b), and (c) are based on 10 years (2007–2016) of daily averaged cross-calibrated multi-platform winds using year-round data. (d) Probability density functions for interstorm periods for winter (June-July-August, blue) and summer (December-January-February, red).

where $f_{\text{heterogeneous}}$ is the fraction of heterogeneous profiles estimated from the fitted float profiles. Assuming $\tau_{\text{mix}} < 1$ day (Brody & Lozier, 2014), we can estimate upper bounds for τ_{bio} from either (1) or (2). The schematic (Figure 8) illustrates vertical profiles over a storm cycle, where τ_{storm}, $\tau_{\text{interstorm}}$, and $\tau_{\text{recurrence}}$ represent median durations for the entire Southern Ocean based on wind speed.

The percentage of time in storm and interstorm conditions from the estimated storm timescales is presented in Table 1, together with percentages of homogeneous and heterogeneous profiles in nighttime Chl-a fluorescence from float data. With the 10 m/s wind speed threshold for storm events, we find that the percentage of time in storm and interstorm conditions in each season agrees well with percentages of sigmoid versus nonsigmoid profiles. This is consistent with bio-optical properties being quickly homogenized in the surface layer during high wind events, but as soon as the wind subsides, gradients in bio-optical properties reform. The extent to which wind-induced mixing penetrates the upper ocean depends on the magnitude and frequency content of the winds, their interactions with mesoscale and submesoscale features, and, ultimately, the mixing processes that are triggered (see, e.g., Dohan & Davis, 2011; Forryan et al., 2015; Whitt, Levy, & Taylor, Whitt, et al., 2017; Whitt & Taylor, 2017).

We also consider homogeneity/heterogeneity in Chl-a fluorescence profiles within the mixed layer, using a constant wind threshold of 10 m/s. All profiles fit by some type of sigmoid that had the depth of the inflection point, and/or subsurface maximum below the MLD was considered homogeneous within the mixed layer. Upper bound estimates of biological timescales of restratification from these profiles ranged between 1 and 3 days (depending on seasonality of storm timescales; see Table 1), which are shorter than typical phytoplankton doubling times inferred from field observations in the region (e.g., de Baar et al., 2005; Latasa et al., 2014;

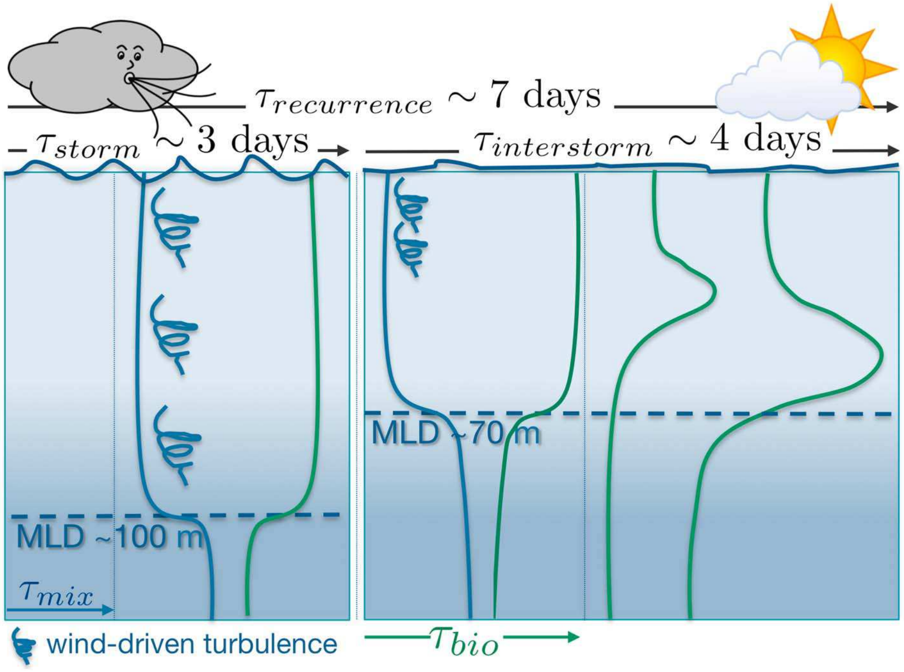

Figure 8. Schematic illustrating the relationship between storm-mixing and biological timescales, with density profiles depicted in blue and Chl-a fluorescence in green. Interstorm periods are on average longer than storm durations, particularly in summer, allowing for bio-optical gradients to form within mixed layers. Storms are defined to have winds $>$ 10m/s. Mixed-layer depth (MLD) estimates for storm and interstorm periods are means from wind-profile matchups and based on the 0.03 kg/m density threshold criterion.

Martin et al., 1990; Nelson & Smith, 1986; Owens et al., 1991; Reay et al., 2001; Sakshaug & Holm-Hansen, 1986; Smetacek et al., 2012) or satellite ocean color (Behrenfeld et al., 2005).

A potential weakness of the 10 m/s threshold for storms is that storm strength could vary locally and seasonally. To take this into account, we also considered a variable threshold for the definition of a storm event: positive wind anomalies or wind speeds higher than the monthly mean at each grid cell. In all seasons, storm timescales based on wind speed anomalies consistently indicate a median duration of ∼3 days for positive and negative wind anomalies, in agreement with satellite wind decorrelation scales (Monahan, 2012), with a recurrence period of ∼6 days. These suggest that half the time the mixed layer is expected to experience active wind forcing, leading to homogenization, and half the time wind-forced mixing would be weak, allowing the formation of gradients. This is consistent with nighttime Chl-a fluorescence profiles showing structure within the mixed layer ∼ 50% of the time in each season (Table 1), suggesting that bio-optical responses to cessation of mixing are immediate.

To identify storm events that could have influenced the upper ocean in 10 days prior to the measured profile, we matched each profile to a 10-day time history of winds at the profile location. Within these time series, storms were identified as events with winds exceeding 10 m/s for at least 3 days. By identifying the last storm prior to the profile, we could estimate the time interval from the conclusion of the last storm to the profile, and we used this information to compute composite averages, binned either by wind speed on the day of the profile or by number of days since the last storm. Results show that stronger winds correspond to deeper mixed layers (Figure 9a) and consistently smaller variance in Chl-a fluorescence and particle backscatter within mixed layers (Figure 9b), as well as smaller Chl-a peak prominences (not shown). Wind speed and MLD decrease within a day or two of the storm (Figure 9c). As expected from storm timescales, winds slightly increase again at day 3 (i.e., median $\tau_{\mathrm{interstorm}}$ for year-round observations) and remain relatively high for the last 3 days of the storm cycle. Consistent with changes in the winds, the SDI for bio-optics (Figure 9d) becomes significantly higher than that at the end of the storm period within 2–3 days of the storm, when bio-optical profiles are expected to be homogenized within the mixed layer. In fact, based on profile fits, ∼70% of bio-optical profiles are homogenized within the mixed layer at the end of a storm; the percentage of homogeneous profiles decreases to ∼50% by the end of the storm cycle (not shown). Under the assumption that the rate of change

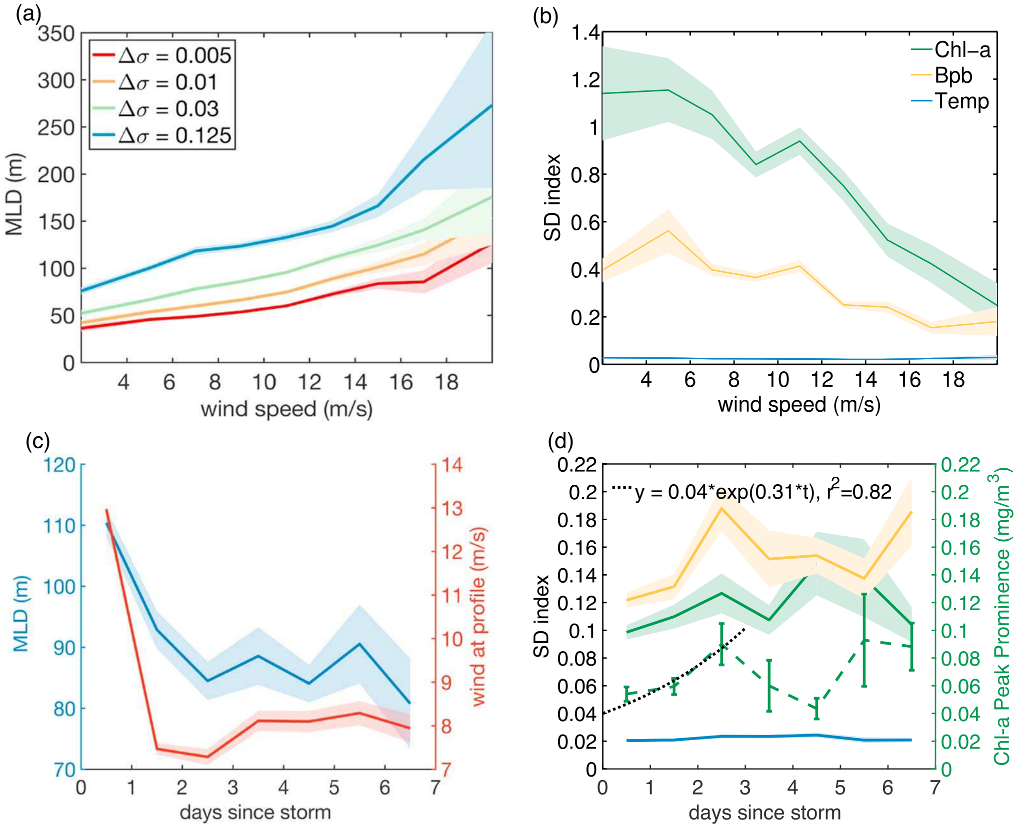

Figure 9. Composites based on wind profile matchups (from daily-averaged winds) binned by wind speed (top row) and time since end of storm period (bottom row). Mean (a) MLD for several density threshold criteria (see legend) and (b) SDI for nighttime Chl-a fluorescence (green), particle backscatter (yellow) and temperature (blue) within the mixed layer, binned by wind speed from year-round observations. (c) Wind speed at the time the profile was sampled (red) and MLD (blue), and (d) SDI for nighttime Chl-a fluorescence (green), particle backscatter (yellow) and temperature (blue), binned by day since the end of the storm period (i.e., days since last time wind was above 10 m/s and persistently high during the previous 3 days). SDIs were normalized by the total standard deviation within mixed layers for high winds in (b), and at the end of a storm period in (d), when mixed layers are more homogeneous (i.e., total variance across mixed-layer observations is minimum). Lines and error bars in (b), (c), and (d) represent means and their mean standard error for all MLD definitions. The dashed green line shows the median peak prominence in Chl-a fluorescence, and the error bar was obtained by bootstrap sampling peak prominences in each bin. The dotted black line shows an exponential fit using observations for the first 3 days since the end of a storm, by means of a weighted least squares approach with 2 degrees of freedom. MLD = mixed-layer depth; SDI = standard deviation index.

of Chl-a peak prominences is proportional to its intensity (see, e.g., Smith et al., 1999), an exponential fit to the first three observations since the end of a storm (dotted black line in Figure 9d)

$$\mathrm{Chla}(t) = \mathrm{Chla}(0)e^{\mu t} \tag{3}$$

allows us to estimate μ, a mean Chl-a-based phytoplankton growth rate (in units of day^{-1}). A linearized weighted least squares approach with $Chla(0) = 0.04$ mg/m^3 (derived from inspection of the intercept from an initial unweighted least squares regression analysis) gives $\mu = 0.31 \pm 0.01$ day^{-1} (or 0.45 doublings day^{-1}). This implies an e-folding timescale for biological restratification of 3.2 ± 0.1 days (i.e., equivalent to a doubling time of 2.2 days), which is on the short end of the range of phytoplankton growth timescales commonly reported from field experiments. If we consider the magnitude of the inhomogeneities detected in bio-optical profiles, with mean Chl-a peak prominences between 0.1 and 0.7 mg/m^3 (Figure 3b), equivalent to increases between 20% and 120% (i.e., relative to the largest neighboring minima, presumably closer to and indicative of surface values), timescales of biological restratification estimated from (3) are between 0.6 and 2.8 days.

Biological timescales of restratification inferred from wind profile matchups (i.e., τ_{bio} ~0.6–2.8 days) are thus consistent with overall statistics (i.e., τ_{bio} <1–3 days, inferred by combining wind and profile structure statistics), despite the inherent inaccuracies of daily-averaged wind analyses (from 6-hourly synoptic winds) assigned to the profile sampling times and the potentially short biological timescales of restratification. Both approaches imply that biological timescales for the formation of vertical bio-optical gradients are shorter than biological timescales for phytoplankton growth inferred for the region from field experiments (from a variety of techniques; e.g., Nelson & Smith, 1986; Reay et al., 2001; Sakshaug & Holm-Hansen, 1986), including in situ iron-addition experiments (e.g., de Baar et al., 2005; Latasa et al., 2014; Martin et al., 1990; Owens et al., 1991; Smetacek et al., 2012) when phytoplankton growth is expected to be enhanced, satellite observations (Behrenfeld et al., 2005, 2008) as well as those simulated by state-of-the-art Earth System models (Rohr et al., 2017). This suggests the possibility that biological timescales for phytoplankton growth in the Southern Ocean might be shorter than commonly thought, in agreement with findings of unusually high maximal growth rates (i.e., between ∼0.3 and 1 day^{-1}) both in the sea ice zone (Smith et al., 1999; Spies, 1987) and in open ocean environments (Priddle et al., 1997; Timmermans et al., 2001, 2004).

6. Summary and Conclusions

New bio-optical data from floats and southern elephant seals reveal that, even in the open Southern Ocean, where harsh year-round weather conditions might be expected to homogenize the upper ocean, subsurface Chl-a fluorescence maxima are common and often occur within hydrographically defined mixed layers.

This study shows clearly that the absence of density stratification in the mixed layer does not imply vertical mixing or vertical homogeneity in other properties, suggesting that turbulence is frequently intermittent within mixed layers. Our results confirm that the MLDs defined by standard density threshold criteria are poor indicators of the active turbulent layer (e.g., Franks, 2014), a conclusion confirmed by microstructure measurements in the Antarctic Polar Front Zone (Cisewski et al., 2005, 2008). Fine-density threshold criteria are usually a better proxy for the depth of active turbulence (e.g., Cisewski et al., 2005; Kilbourne & Girton, 2015). However, fine-density threshold criteria are more sensitive to measurement errors and require higher vertical resolution within the mixed layer.

These observations suggest that it is often incorrect to assume that biogeochemical tracers are well mixed in a hydrographically defined mixed layer. Including heterogeneity in bio-optical properties and plankton within mixed layers is important, for example, when correcting NPQ effects in daytime Chl-a fluorescence. Methods that assume homogeneity within the mixed layer (e.g., Xing et al., 2012) will miss real subsurface features within the mixed layer and will lead to incorrect estimates of the integrated stock of Chl-a fluorescence. Alternative methods to overcome the assumption of homogeneity within the mixed layer have been proposed (e.g., Biermann et al., 2015) and are encouraged.

Southern Ocean DFM, although not as intense as subsurface Chl-a fluorescence maxima found in subtropical regions (e.g., Letelier et al., 2004; Mignot et al., 2014), can occur in all seasons, albeit with higher frequency of occurrence in summer. DFM are often found at or near the base of the MLD, underscoring the importance of physical mechanisms in the formation and maintenance of DFM. Although the shape of bio-optical profiles may provide insights into the underlying mechanisms of formation and maintenance of DFM layers (e.g., Cullen, 2015; Durham & Stocker, 2012; Prairie et al., 2011), identifying those mechanisms requires data that are unavailable from autonomous platforms, and it is outside the scope of this study. Most notably, nighttime DFM are often found above the MLD, indicating the existence of biological gradients within the hydrographic mixed layer.

The existence of gradients in nighttime Chl-a fluorescence within mixed layers is consistent with the timescale for biological restratification (e.g., growth or adaptation to the light gradient) being shorter than the timescale associated with homogenizing physical properties within the mixed layer. Although the existence of Chl-a fluorescence gradients can result from physiological adaptation to ambient light and does not necessarily imply gradients in phytoplankton biomass (e.g., Cullen & Eppley, 1981), horizontal variability in nighttime Chl-a fluorescence in the Southern Ocean appears correlated with phytoplankton biomass (Strutton et al., 1997), and phytoplankton can be unevenly distributed even in deep winter mixed layers (Backhaus et al., 2003; Lacour et al., 2017; Ryther & Hulburt, 1960).

We hypothesize that intermittent atmospheric forcing may allow for periods of quiescence and reduced turbulence in deep mixed layers between storm events, allowing the formation of DFM and/or Chl-a unevenness within the seasonal mixed layer. Satellite wind data indicate that the median duration of a storm, defined as a wind event with wind speeds higher than 10 m/s, is ∼ 3–4 days. Storm timescales exhibit seasonality:

storms are slightly less frequent in summer (one storm arrival every 8 days) and with longer interstorm periods (~ 5 days). The median interstorm period is 3–5 days (depending on season), implying that biological restratification must occur on timescales shorter than 3–5 days.

We have discussed a means of constraining biological timescales of restratification from storm-mixing timescales (storm recurrence, duration, and interstorm period), combining overall statistics of satellite winds and bio-optical profile structure. Wind-profile matchups, although subject to larger uncertainties, are in agreement with overall statistics. Our analyses suggest that biological timescales of restratification imply a phytoplankton doubling time of about 2.2 days, which is a bit shorter than typical doubling times for the region estimated from field observations, satellite ocean color, or Earth System models (i.e., $> 3-4$ days; e.g., Rohr et al., 2017). The findings underscore the fact that heterogeneity is detectable long before phytoplankton populations have doubled. Phytoplankton growth rates inferred from this analysis are consistent with rates >0.3 day^{-1} that have been reported in Antarctic waters influenced by sea ice (e.g. Smith et al., 1999; Spies, 1987), and though unusual for open ocean waters of the Southern Ocean, they are not unprecedented in field observations (Priddle et al., 1997; Timmermans et al., 2001, 2004). Short biological timescales for growth, comparable to those typical of coastal or upwelling systems, suggest that phytoplankton populations in the Southern Ocean are well adapted to the low temperatures, irradiance, and iron conditions (Banse, 1991; Furnas, 1990). Our results suggest that unless there is a storm event, biological structure can be detected in the upper ocean and mixed layer, in agreement with the study by Therriault and Platt (1978) from observations in the coastal ocean. Our results also suggest that biological processes frequently dominate vertical mixing in the mixed layer. The high degree of variance we observe in mixed layer nighttime Chl-a fluorescence and particle backscatter statistics is not observed in hydrographic properties.

To the extent that nighttime Chl-a fluorescence is proportional to phytoplankton biomass, we hypothesize that the seasonality in storm timescales will impact phytoplankton bloom development, with longer interstorm periods allowing sufficient time for gradients and DFM to develop, particularly in the summer. Subsequent storms may increase surface concentrations of Chl-a, by deepening the mixed layer and entraining limiting nutrients and/or Chl-a into the mixed layer (e.g., Carranza & Gille, 2015; Marra et al., 1990; Rumyantseva et al., 2015; Whitt et al., 2017) and/or by homogenizing Chl-a within the mixed layer. Seasonal differences between storm and interstorm periods suggest that atmospheric synoptic-scale variability might have an impact on seasonal and longer timescales. As proposed by Legendre (1981), the alternation of periods of stratification and destratification enhances primary production across multiple scales and phenomena. Our results suggest that the frequency of storm cycles (storm and interstorm periods and their relative duration) might control net phytoplankton production in the Southern Ocean.

As more biogeochemical floats are released in the Southern Ocean, it may be possible to assess the relative contributions of spatial and temporal variance to total variance in bio-optical properties (see, e.g., Therriault & Platt, 1978) within Southern Ocean mixed layers. Concurrent high-resolution observations of atmospheric forcing (i.e., buoyancy fluxes and winds), in situ turbulence measurements, and water column bio-optical properties and other biogeochemical tracers (e.g., nitrate and oxygen data also available from the floats but not from the elephant seals) will be key to assessing the hypotheses put forward by the present study.

Appendix A : Profile Fits

The equations for the functional forms fit to the profile data are derived from those presented by Mignot et al. (2011). These are a sigmoid (a)

$$F(z) = \frac{F_{\mathrm{surf}}}{1 + e^{(Z_{1/2} - z)s}}, \tag{A1}$$

with $m = 3$ coefficients: a surface value, F_{surf}, the depth where the surface value reduces to one half, $Z_{1/2}$, and the sigmoid fit slope at $Z_{1/2}$, s; an exponential (b)

$$F(z) = F_{\mathrm{surf}} e^{-\frac{\ln 2}{Z_{1/2}} z}, \tag{A2}$$

with $m = 2$ coefficients: F_{surf} and $Z_{1/2}$; a Gaussian (c)

$$F(z) = F_{max} e^{-\frac{(z-Z_{\max})^2}{\mathrm{d}z^2}}, \tag{A3}$$

with $m = 3$ coefficients: the maximum value $F_{\max}$, the depth of the maximum $Z_{\max}$, and a proxy for the maximum thickness, dz; a linear combination of a Gaussian with an exponential (d)

$$F(z) = F_{\mathrm{surf}} e^{-\frac{\ln 2}{Z_{1/2}} z} + F_{\max} e^{-\frac{(z-Z_{\max})^2}{\mathrm{d}z^2}}, \tag{A4}$$

with $m = 5$ coefficients: F_{surf}, $Z_{1/2}$, $Z_{\max}$, $F_{\max}$, and dz and a linear combination of a Gaussian with a sigmoid (e)

$$F(z) = \frac{F_{\mathrm{surf}}}{1 + e^{(Z_{1/2}-z)*s}} + F_{\max} e^{-\frac{(z-Z_{\max})^2}{\mathrm{d}z^2}}, \tag{A5}$$

with $m = 6$ coefficients: F_{surf}, $Z_{1/2}$, s, $Z_{\max}$, $F_{\max}$, and dz.

The nonlinear least squares fitting procedure uses an iterative approach that requires initial guesses for the fitted parameters (implemented using the fit.m function in MATLAB R2016a). First guesses for fitted parameters (i.e., F_{surf}, $Z_{1/2}$, $Z_{\max}$, $F_{\max}$, and dz) were chosen based on the observed profiles. For F_{surf}, we used the mean for the top 30 m. For the depth of the inflection point, $Z_{1/2}$, we use the depth at which the surface value was reduced by half or the MLD (using Holte & Talley's, 2009 algorithm), whichever was deepest. For Gaussian models, the depth and magnitude of the maximum ($Z_{\max}$ and $F_{\max}$) were chosen based on the most prominent peak (i.e., the greatest peak relative to the largest neighboring minima, using the MATLAB built-in function findpeaks.m) if greater than the instrument noise level (i.e., 0.02 mg/m^3); otherwise, the depth of the absolute maximum was chosen. The peak width was initially set to 5 m for float data and 10 m for seal data. With this choice of initial parameters the fitting algorithm most often converged to a solution (albeit with exceptions in which peak width needed to be adjusted to a larger value) and visual inspection of all profile fits looked reasonable. Gaussian fits were most sensitive to the initial parameters for the maximum, and by choosing those based on the most prominent peak (instead of the absolute maximum) we were able to capture structure and fit maxima near the base of the mixed layer and avoid fitting less prominent maxima (though largest in absolute magnitude) close to the surface and/or Gaussians with maxima at the surface.

Acknowledgments
This work was funded by the NASA NESFF fellowship (NNX12AN41H 001), by NASA (NNX08AI82G, NNX14A078G, NNX14A078G, NNX13AE44G and NNX17AH53G), and by NSF grants (ARRA OCE0850350, ANT-0948338 and OCE-1658001). This work was also sponsored by NSF's Southern Ocean Carbon and Climate Observations and Modeling (SOCCOM) Project under the NSF award PLR-1425989 with additional support from NOAA and NASA. Logistical support for this project in Antarctica was provided by the U.S. National Science Foundation through the U.S. Antarctic Program. We thank all the people involved in the calibration, deployment, and acquisition of subsurface Chl-a data used in this study and for making it available to the science community. Thanks to the DIMES project for the deployment of EM-APEX floats (NSF grant OCE-1129564), MBARI, and SOCCOM for collecting and making the float data freely available (http://soccom.princeton.edu/content/soccom-observations). Southern elephant seal data were downloaded from www.earth-syst-sci-data.net/5/15/2013/doi:10.5194/essd-5-15-2013, and bio-optical data from biogeochemical Argo floats are available at http://www.mbari.org/chemsensor/floatviz.htm. CCMP Version-2.0 vector wind analyses are produced by Remote Sensing Systems and are available at www.remss.com/measurements/ccmp. We thank James Holte for his MATLAB code to estimate MLD, available at http://mixedlayer.ucsd.edu. The MATLAB function used to estimate sunrise and sunset times is available at http://mooring.ucsd.edu/software/matlab/doc/toolbox/geo/suncycle.html. Finally, we thank Emmanuel Boss for his input to an earlier draft of this manuscript and constructive comments from two anonymous reviewers that helped to improve the presentation of the manuscript.

References

Abraham, E. R. (1998). The generation of plankton patchiness by turbulent stirring. *Nature*, *391*(6), 577–580.

Adams, K. A., Hosegood, P., Taylor, J. R., Sallée, J.-B., Bachman, S., Torres, R., et al. (2017). Frontal circulation and submesoscale variability during the formation of a Southern Ocean mesoscale eddy. *Journal of Physical Oceanography*, *47*(7), 1737–1753.

Atlas, R., Hoffman, R. N., Ardizzone, J., Leidner, S. M., Jusem, J. C., Smith, D. K., et al. (2011). A cross-calibrated, multiplatform ocean surface wind velocity product for meteorological and oceanographic applications. *Bulletin of the American Meteorological Society*, *92*(2), 157–174.

Bachman, S. D., Taylor, J. R., Adams, K. A., & Hosegood, P. J. (2017). Mesoscale and submesoscale effects on mixed layer depth in the Southern Ocean. *Journal of Physical Oceanography*, *47*(9), 2173–2188.

Backhaus, J. O., Hegseth, E. N., Wehde, H., Irigoien, X., Hatten, K., & Logemann, K. (2003). Convection and primary production in winter. Marine ecology progress series. *Oldendorf*, *251*, 1–14.

Banse, K. (1991). Rates of phytoplankton cell division in the field and in iron enrichment experiments. *Limnology and Oceanography*, *36*, 1886–1898.

Beckmann, A., & Hense, I. (2007). Beneath the surface: Characteristics of oceanic ecosystems under weak mixing conditions—A theoretical investigation. *Progress In Oceanography*, *75*(4), 771–796.

Behrenfeld, M. J., & Boss, E. (2003). The beam attenuation to chlorophyll ratio: An optical index of phytoplankton physiology in the surface ocean? *Deep Sea Research Part I: Oceanographic Research Papers*, *50*(12), 1537–1549.

Behrenfeld, M., & Boss, E. (2006). Beam attenuation and chlorophyll concentration as alternative optical indices of phytoplankton biomass. *Journal of Marine Research*, *64*(3), 431–451.

Behrenfeld, M., Boss, E., Siegel, D., & Shea, D. (2005). Carbon-based ocean productivity and phytoplankton physiology from space. *Global Biogeochemical Cycles*, *19*, GB1006. https://doi.org/10.1029/2004GB002299

Behrenfeld, M. J., Halsey, K. H., & Milligan, A. J. (2008). Evolved physiological responses of phytoplankton to their integrated growth environment. *Philosophical Transactions: Biological Sciences*, *363*(1504), 2687–2703.

Belcher, S. E., Grant, A. L. M., Hanley, K. E., Fox-Kemper, B., Van Roekel, L., Sullivan, P. P., et al. (2012). A global perspective on Langmuir turbulence in the ocean surface boundary layer. *Geophysical Research Letters*, *39*, L18605. https://doi.org/10.1029/2012GL052932

Biermann, L., Guinet, C., Bester, M., Brierley, A., & Boehme, L. (2015). An alternative method for correcting fluorescence quenching. *Ocean Science*, *11*(1), 83–91.

Biuw, M., Boehme, L., Guinet, C., Hindell, M., Costa, D., Charrassin, J.-B., et al. (2007). Variations in behavior and condition of a Southern Ocean top predator in relation to in situ oceanographic conditions. *Proceedings of the National Academy of Sciences of the United States of America*, *104*(34), 13,705–13,710.

Boss, E. B., & Haentjens, N. (2016). Primer regarding measurements of chlorophyll fluorescence and the backscattering coefficient with WETLabs FLBB on profiling floats (SOCCOM Technical Report 2016-1). Princeton, NJ: SOCCOM, Princeton University.

Boss, E., & Pegau, W. S. (2001). Relationship of light scattering at an angle in the backward direction to the backscattering coefficient. *Applied Optics*, *40*(30), 5503–5507.

Brainerd, K. E., & Gregg, M. C. (1995). Surface mixed and mixing layer depths. *Deep-Sea Research Part I*, *42*(9), 1521–1543.

Briggs, N., Perry, M. J., Cetinić, I., Lee, C., D'Asaro, E., Gray, A. M., et al. (2011). High-resolution observations of aggregate flux during a sub-polar North Atlantic spring bloom. *Deep-Sea Research Part I*, *58*(10), 1031–1039.

Brody, S. R., & Lozier, M. S. (2014). Chages in dominant mixing length scales as a driver of subpolar phytoplankton bloom initiation in the North Atlantic. *Geophysical Research Letters*, *41*, 3197–3203. https://doi.org/10.1002/2014GL059707

Callies, J., Flierl, G., Ferrari, R., & Fox-Kemper, B. (2015). The role of mixed-layer instabilities in submesoscale turbulence. *Journal of Fluid Mechanics*, *788*, 5–41.

Campbell, J. (1995). The lognormal distribution as a model for bio-optical variability in the sea. *Journal of Geophysical Research*, *100*(C7), 13,237–13,254.

Campbell, J. W., & O'Reilly, J. E. (2006). Metrics for quantifying the uncertainty in a chlorophyll algorithm: Explicit equations and examples using the OC4. v4 algorithm and NOMAD data, Ocean Color Bio-optical Algorithm Mini-Workshop (27-29 September) (pp. 2005).

Carranza, M. M., & Gille, S. T. (2015). Southern Ocean wind-driven entrainment enhances satellite chlorophyll-a through the summer. *Journal of Geophysical Research: Oceans*, *120*, 304–323. https://doi.org/10.1002/2014JC010203

Charrassin, J.-B., Hindell, M., Rintoul, S. R., Roquet, F., Sokolov, S., Biuw, M., et al. (2008). Southern Ocean frontal structure and sea-ice formation rates revealed by elephant seals. *Proceedings of the National Academy of Sciences of the United States of America*, *105*(33), 11,634–11,639.

Charrassin, J.-B., Roquet, F., Park, Y. H., Bailleul, F., Guinet, C., Meredith, M., et al. (2010). New insights into Southern Ocean physical and biological processes revealed by instrumented elephant seals. In J. Hall, D. E. Harrison, & D. Stammer (Eds.), *Proceedings of OceanObs 09: Sustained ocean observations and information for society, September 2009* (Vol. 2, pp. 21–25). Venice, Italy: ESA Publication WPP-306.

Chiswell, S. (2011). Annual cycles and spring blooms in phytoplankton: Don't abandon Sverdrup completely. *Marine Ecology Progress Series*, *443*, 39–50.

Cisewski, B., Strass, V. H., Losch, M., & Prandke, H. (2008). Mixed layer analysis of a mesoscale eddy in the Antarctic Polar Front Zone. *Journal of Geophysical Research*, *113*, C05017. https://doi.org/10.1029/2007JC004372

Cisewski, B., Strass, V. H., & Prandke, H. (2005). Upper-ocean vertical mixing in the Antarctic Polar Front Zone. *Deep Sea Research Part II: Topical Studies in Oceanography*, *52*(9-10), 1087–1108.

Claustre, H., Kerhervé, P., Marty, J. C., & Prieur, L. (1994). Phytoplankton photoadaptation related to some frontal physical processes. *Journal of Marine Systems*, *5*(3), 251–265.

Cole, S. T., Rudnick, D. L., & Colosi, J. A. (2010). Seasonal evolution of upper-ocean horizontal structure and the remnant mixed layer. *Journal of Geophysical Research*, *115*, C04012. https://doi.org/10.1029/2009JC005654

Cullen, J. J. (1982). The deep chlorophyll maximum: Comparing vertical profiles of chlorophyll a. *Canadian Journal of Fisheries and Aquatic Sciences*, *39*(5), 791–803.

Cullen, J. J. (2015). Subsurface chlorophyll maximum layers: Enduring enigma or mystery solved? *Annual Review of Marine Science*, *7*(1), 207–239.

Cullen, J. J., & Eppley, R. W. (1981). Chlorophyll maximum layers of the Southern-California Bight and possible mechanisms of their formation and maintenance. *Oceanologica Acta*, *4*(1), 23–32.

Cullen, J., & Lewis, M. R. (1988). The kinetics of algal photoadaptation in the context of vertial mixing. *Journal of Plankton Research*, *10*, 1039–1063.

Currie, W. J. S., & Roff, J. C. (2006). Plankton are not passive tracers: Plankton in a turbulent environment. *Journal of Geophysical Research*, *111*, C05S07. https://doi.org/10.1029/2005JC002967

D'Asaro, E., Lee, C., Rainville, L., Harcourt, R., & Thomas, L. (2011). Enhanced turbulence and energy dissipation at ocean fronts. *Science*, *332*(6027), 318–322.

Davis, R. E., Ohman, M. D., Rudnick, D. L., & Sherman, J. T. (2008). Glider surveillance of physics and biology in the southern California Current System. *Limnology and Oceanography*, *53*, 2151–2168.

de Baar, H. J. W. d., Boyd, P. W., Coale, K. H., Landry, M. R., Tsuda, A., Assmy, P., et al. (2005). Synthesis of iron fertilization experiments: From the Iron Age in the Age of Enlightenment. *Journal of Geophysical Research*, *110*, C09S16. https://doi.org/10.1029/2004JC002601

de Boyer, Montégut, C., Madec, G., Fischer, A. S., Lazar, A., & Iudicone, D. (2004). Mixed layer depth over the global ocean: An examination of profile data and a profile-based climatology. *Journal of Geophysical Research*, *109*, C12003. https://doi.org/10.1029/2004JC002378

Del Castillo, C. E., & Miller, R. L. (2011). Horizontal and vertical distributions of colored dissolved organic matter during the Southern Ocean gas exchange experiment. *Journal of Geophysical Research*, *116*, C00F07. https://doi.org/10.1029/2010JC006781

Denman, K. (1983). Time and space scales of vertical mixing and advection of phytoplankton in the upper ocean. *Limnology and Oceanography*, *28*, 801–815.

Denman, K., & Gargett, A. (1995). Biological-physical interactions in the upper ocean: The role of vertical and small scale transport processes. *Annual Review of Fluid Mechanics*, *27*(1), 225–256.

Dierssen, H. M. (2010). Perspectives on empirical approaches for ocean color remote sensing of chlorophyll in a changing climate. *Proceedings of the National Academy of Sciences*, *107*(40), 17,073–17,078.

Djavidnia, S., Mélin, F., & Hoepffner, N. (2010). Comparison of global ocean colour data records. *Ocean Science*, *6*, 61–76.

Dohan, K., & Davis, R. E. (2011). Mixing in the transition layer during two storm events. *Journal of Physical Oceanography*, *41*(1), 42–66.

Dong, S., Sprintall, J., Gille, S. T., & Talley, L. (2008). Southern Ocean mixed-layer depth from Argo float profiles. *Journal of Geophysical Research*, *113*, C06013. https://doi.org/10.1029/2006JC004051

Dorsch, W., Newland, T., Tassone, D., Tymons, S., & Walker, D. (2008). A statistical approach to modelling the temporal patterns of ocean storms. *Journal of Coastal Research*, *246*, 1430–1438.

Dragon, A.-C., Monestiez, P., Bar-Hen, A., & Guinet, C. (2010). Linking foraging behaviour to physical oceanographic structures: Southern elephant seals and mesoscale eddies east of Kerguelen Islands. *Progress In Oceanography*, *87*(1-4), 61–71.

du Plessis, M., Swart, S., Ansorge, I. J., & Mahadevan, A. (2017). Submesoscale processes promote seasonal restratification in the Subantarctic Ocean. *Journal of Geophysical Research: Oceans*, *122*, 2960–2975. https://doi.org/10.1002/2016JC012494

Durham, W. M., & Stocker, R. (2012). Thin phytoplankton layers: Characteristics, mechanisms, and consequences. *Annual Review of Marine Science*, *4*(1), 177–207.

Dusenberry, J (2000). Steady-state single cell model simulations of photoacclimation in a vertically mixed layer: Implications for biological tracer studies and primary productivity. *Journal of Marine Systems*, *24*, 201–220.

Dusenberry, J., & Olson, R. J. (1999). Frequency distributions of phytoplankton single? Cell fluorescence and vertical mixing in the surface ocean. *Limnology and Oceanography*, *44*(2), 431–435.

Eagleson, P. S. (1978). Climate, soil, and vegetation. 2. Distribution of annual precipitation derived from observed storm sequences. *Water Resources Research*, *14*(5), 713–721.

Erickson, Z. K., Thompson, A. F., Cassar, N., Sprintall, J., & Mazloff, M. R. (2016). An advective mechanism for deep chlorophyll maxima formation in southern Drake Passage. *Geophysical Research Letters*, *43*, 1–10. https://doi.org/10.1002/2016GL070565

Falkowski, b. P. G. (1983). Light-shade adaptation and vertical mixing of marine phytoplankton: A comparative field study. *Journal of Marine Research*, *41*, 215–237.

Fedak, M. A. (2013). The impact of animal platforms on polar ocean observation. *Deep Sea Research Part II*, *88-89*, 7–13.

Forryan, A., Naveira Garabato, A. C., Polzin, K. L., & Waterman, S. (2015). Rapid injection of near-inertial shear into the stratified upper ocean at an Antarctic Circumpolar Current front. *Geophysical Research Letters*, *42*, 3431–3441. https://doi.org/10.1002/2015GL063494

Fox-Kemper, B., Danabasoglu, G., Ferrari, R., Griffies, S. M., Hallberg, R., Holland, M. M., et al. (2011). Parameterization of mixed layer eddies. III: Implementation and impact in global ocean climate simulations. *Ocean Modelling*, *39*(1-2), 61–78.

Fox-Kemper, B., Ferrari, R., & Hallberg, R. (2008). Parameterization of mixed layer eddies. Part I: Theory and diagnosis. *Journal of Physical Oceanography*, *38*(6), 1145–1165.

Franks, P. J. S. (2014). Has Sverdrup's critical depth hypothesis been tested? Mixed layers vs. turbulent layers. *ICES Journal of Marine Science*, *72*, 1897–1907. https://doi.org/10.1093/icesjms/fsu175

Franks, P., & Marra, J. (1994). A simple new formulation for phytoplankton photoresponse and an application in a wind-driven mixed-layer model. *Marine Ecology Progress Series*, *111*(1), 143–153.

Franks, P. J. S., & Walstad, L. J. (1997). Phytoplankton patches at fronts: A model of formation and response to wind events. *Journal of Marine Research*, *55*(1), 1–29.

Frenger, I., Münnich, M., Gruber, N., & Knutti, R. (2015). Southern Ocean eddy phenomenology. *Journal of Geophysical Research: Oceans*, *120*, 7413–7449. https://doi.org/10.1002/2015JC011047

Furnas, M. J. (1990). In situ growth rates of marine phytoplankton: Approaches to measurement, community and species growth rates. *Journal of Plankton Research*, *12*, 1117–1151.

Gardner, W. D., Chung, S. P., Richardson, M. J., & Walsh, I. D. (1995). The oceanic mixed-layer pump. *Deep Sea Research Part II: Topical Studies in Oceanography*, *42*, 757–765.

Gomi, Y., Fukuchi, M., & Taniguchi, A. (2010). Diatom assemblages at subsurface chlorophyll maximum layer in the eastern Indian sector of the Southern Ocean in summer. *Journal of Plankton Research*, *32*(7), 1039–1050.

Gong, X., Shi, J., Gao, H. W., & Yao, X. H. (2015). Steady-state solutions for subsurface chlorophyll maximum in stratified water columns with a bell-shaped vertical profile of chlorophyll. *Biogeosciences*, *12*(4), 905–919.

Grenier, M., Della Penna, A., & Trull, T. W. (2015). Autonomous profiling float observations of the high-biomass plume downstream of the Kerguelen Plateau in the Southern Ocean. *Biogeosciences*, *12*(9), 2707–2735.

Griffith, G. P., Vennell, R., & Williams, M. J. M. (2010). An algal photoprotection index and vertical mixing in the Southern Ocean. *Journal of Plankton Research*, *32*(4), 515–527.

Guinet, C., Xing, X., Walker, E., & Monestiez, P. (2013). Calibration procedures and first dataset of Southern Ocean chlorophyll a profiles collected by elephant seals equipped with a newly developed CTD-fluorescence tags. *Earth System Science Data*, *5*, 15–29.

Håkanson, L., Malmaeus, J. M., Bodemer, U., & Gerhardt, V. (2003). Coefficients of variation for chlorophyll, green algae, diatoms, cryptophytes and blue-greens in rivers as a basis for predictive modelling and aquatic management. *Ecological modelling*, *169*(1), 179–196.

Haëntjens, N., Boss, E., & Talley, L. D. (2017). Revisiting Ocean Color algorithms for chlorophyll a and particulate organic carbon in the Southern Ocean using biogeochemical floats. *Journal of Geophysical Research: Oceans*, *122*, 6583–6593. https://doi.org/10.1002/2017JC012844

Hodges, K. I., & Lee, R. W. (2011). B. L A comparison of extratropical cyclones in recent reanalyses ERA-Interim, NASA MERRA, NCEP CFSR, and JRA-25. *Journal of Climate*, *24*(18), 4888–4906.

Holm-Hansen, O., Amos, A. F., & Hewes, C. D. (2000). Reliability of estimating chlorophyll a concentrations in Antarctic waters by measurement of in situ chlorophyll a fluorescence. *Marine Ecology–Progress Series*, *196*, 103–110.

Holm-Hansen, O., & Hewes, C. D. (2004). Deep chlorophyll-a maxima (DCMs) in Antarctic waters. I. Relationships between DCMs and the physical, chemical, and optical conditions in the upper water column. *Polar Biology*, *27*(11), 699–710. https://doi.org/10.1007/s00300-004-0641-1

Holm-Hansen, O., Kahru, M., & Hewes, C. D. (2005). Deep chlorophyll a maxima (DCMs) in pelagic Antarctic waters. II. Relation to bathymetric features and dissolved iron concentrations. *Marine Ecology–Progress Series*, *297*, 71–81.

Holte, J., & Talley, L. (2009). A new algorithm for finding mixed layer depths with applications to Argo data and Subantarctic Mode Water formation. *Journal of Atmospheric and Oceanic Technology*, *26*(9), 1920–1939.

Holte, J. W., Talley, L. D., Chereskin, T. K., & Sloyan, B. M. (2012). The role of air-sea fluxes in Subantarctic Mode Water formation. *Journal of Geophysical Research*, *117*, C03040. https://doi.org/10.1029/2011JC007798

Hopkinson, B., Mitchell, B. G., & Reynolds, R. (2007). Iron limitation across chlorophyll gradients in the southern Drake Passage: Phytoplankton responses to iron addition and photosynthetic indicators of iron stress. *Limnology and Oceanography*, *52*, 2540–2554. https://doi.org/10.4319/lo.2007.52.6.2540

Huisman, J., van Oostveen, P., & Weissing, F. (1999). Critical depth and critical turbulence: Two different mechanisms for the development of phytoplankton blooms. *Limnology and Oceanography*, *44*, 1781–1787.

IOCCG (2015). Ocean Colour Remote Sensing in Polar. In M. Babin, K. Arrigo, S. Bélanger, & M.–H. Forget (Eds.), *IOCCG report series, no. 16, International Ocean Colour Coordinating Group*. Dartmouth, Canada.

Iudicone, D., Rodgers, K. B., Plancherel, Y., Aumont, O., Ito, T., Key, R. M., et al. (2016). The formation of the ocean's anthropogenic carbon reservoir. *Scientific Reports*, *6*(35473). https://doi.org/10.1038/srep35473

Jaud, T., Dragon, A.-C., Garcia, J. V., & Guinet, C. (2012). Relationship between Chlorophyll a concentration, light attenuation and diving depth of the southern elephant seal Mirounga leonina. *PLoS ONE*, *7*(10), e47444. https://doi.org/10.1371/journal.pone.0047444

Johnson, K. S., Plant, J. N., Coletti, L. J., Jannasch, H. W., Sakamoto, C. M., Riser, S. C., et al. (2017). Biogeochemical sensor performance in the SOCCOM profiling float array. *Journal of Geophysical Research: Oceans*, *122*, 6416–6436. https://doi.org/10.1002/2017JC012838

Kilbourne, B. F., & Girton, J. B. (2015). Surface boundary layer evolution and near-inertial wind power input. *Journal of Geophysical Research: Oceans*, *120*, 7506–7520.

Kolber, Z. S., Prasil, O., & Falkowski, P. G. (1998). Measurements of variable chlorophyll fluorescence using fast repetition rate techniques: Defining methodology and experimental protocols. *Biochimica Et Biophysica Acta-Bioenergetics*, *1367*(1-3), 88–106.

Lacour, L., Ardyna, M., Stec, K. F., Claustre, H., Prieur, L., Poteau, A., et al. (2017). Unexpected winter phytoplankton blooms in the North Atlantic subpolar gyre. *Nature Geoscience*, *10*(11), 836–839.

Latasa, M., Henjes, J., Scharek, R., Assmy, P., Röttgers, R., & Smetacek, V. (2014). Progressive decoupling between phytoplankton growth and microzooplankton grazing during an iron-induced phytoplankton bloom in the Southern Ocean (EIFEX). *Marine Ecology Progress Series*, *513*, 39–50.

Lavigne, H., D'Ortenzio, F., Ribera D'Alcalà, M., Claustre, H., Sauzède, R., & Gacic, M. (2015). On the vertical distribution of the chlorophyll a concentration in the Mediterranean Sea: A basin-scale and seasonal approach. *Biogeosciences*, *12*(16), 5021–5039.

Ledwell, J. R., St Laurent, L. C., Girton, J. B., & Toole, J. M. (2011). Diapycnal mixing in the Antarctic Circumpolar Current. *Journal of Physical Oceanography*, *41*(1), 241–246.

Legendre, L. (1981). Hydrodynamic control of marine phytoplankton production: The paradox of stability++contribution to the programme of giroq GIROQ (Groupe interuniversitaire de recherches océanographiques du Québec). In J. C. J. Nihoul (Eds.), *Ecohydrodynamics, Elsevier Oceanography Series* (Vol. 32, pp. 191–207). Elsevier. https://doi.org/10.1016/S0422-9894(08)70410-0

Letelier, R. M., Karl, D. M., Abbott, M. R., & Bidigare, R. R. (2004). Light driven seasonal patterns of chlorophyll and nitrate in the lower euphotic zone of the North Pacific Subtropical Gyre. *Limnology and Oceanography*, *49*, 508–519.

Lévy, M., Ferrari, R., Franks, P. J. S., Martin, A. P., & Rivière, P. (2012). Bringing physics to life at the submesoscale. *Geophysical Research Letters*, *39*, L14602. https://doi.org/10.1029/2012GL052756

Lewis, M. R., Cullen, J. J., & Platt, T. R. (1984). Relationships between vertical mixing and photoadaptation of phytoplankton: Similarity criteria. *Marine Ecology Progress Series*, *15*, 141–149.

Lewis, M. R., Horne, E. P. W., Cullen, J. J., Oakey, N. S., & Platt, T. (1984). Turbulent motions may control phytoplankton photosynthesis in the upper ocean. *Nature*, *311*(5), 49–50.

Long, M. C., Thomas, L. N., & Dunbar, R. B. (2012). Control of phytoplankton bloom inception in the Ross Sea, Antarctica, by Ekman restratification. *Global Biogeochemical Cycles*, *26*, GB1006. https://doi.org/10.1029/2010GB003982

Mackas, D. L., Denman, K. L., & Abott, M. R. (1985). Plankton patchiness: Biology in the physical vernacular. *Bulletin of Marine Science*, *37*(2), 652–674.

MacIntyre, S. (2008). Turbulent mixing and resource supply to phytoplankton, physical processes in lakes and oceans. *Coastal and Estuarine Studies*, *54*, 561–590.

Mahadevan, A., & Campbell, J. (2002). Biogeochemical patchiness at the sea surface. *Geophysical Research Letters*, *29*(19), 1926. https://doi.org/10.1029/2001GL014116

Mahadevan, A., & Campbell, J. (2003). Biogeochemical variability at the sea surface: How it is linked to process response times, Handbook of Scaling Methods in Aquatic Ecology: Measurement, Analysis Simulation (pp. 215–227).

Mahadevan, A., D'Asaro, E., Lee, C., & Perry, M. J. (2012). Eddy-driven stratification initiates north atlantic spring phytoplankton blooms. *Science*, *337*(6090), 54–58.

Mahadevan, A., Tandon, A., & Ferrari, R. (2010). Rapid changes in mixed layer stratification driven by submesoscale instabilities and winds. *Journal of Geophysical Research*, *115*, C03017. https://doi.org/10.1029/2008JC005203

Marra, J. (1978). Phytoplankton photosynthetic response to vertical movement in a mixed layer. *Marine Biology*, *46*, 203–208.

Marra, J., Bidigare, R., & Dickey, T. (1990). Nutrients and mixing, chlorophyll and phytoplankton growth. *Deep Sea Research*, *37*, 127–143.

Martin, J., Fitzwater, S., & Gordon, R. (1990). Iron deficiency limits phytoplankton growth in Antarctic waters. *Global Biogeochemical Cycles*, *4*, 5–12.

Martinez-Vicente, V., Dall'Olmo, G., Tarran, G., Boss, E., & Sathyendranath, S. (2013). Optical backscattering is correlated with phytoplankton carbon across the Atlantic Ocean. *Geophysical Research Letters*, *40*, 1154–1158. https://doi.org/10.1002/grl.50252

McDougall, T. J., & Barker, P. M. (2011). Getting started with TEOS-10 and the Gibbs Seawater (GSW) Oceanographic Toolbox, SCOR/IAPSO WG127, pp. 1–34.

McWilliams, J. C., Huckle, E., Liang, J., & Sullivan, P. P. (2014). Langmuir turbulence in swell. *Journal of Physical Oceanography*, *44*(3), 870–890.

Mignot, A., Claustre, H., D'Ortenzio, F., Xing, X., Poteau, A., & Ras, J. (2011). From the shape of the vertical profile of in vivo fluorescence to Chlorophyll-a concentration. *Biogeosciences*, *8*(8), 2391–2406.

Mignot, A., Claustre, H., Uitz, J., Poteau, A., D'Ortenzio, F., & Xing, X. (2014). Understanding the seasonal dynamics of phytoplankton biomass and the deep chlorophyll maximum in oligotrophic environments: A Bio-Argo float investigation. *Global Biogeochemical Cycles*, *28*, 856–876. https://doi.org/10.1002/2013GB004781

Mitchell, B. G., & Kiefer, D. A. (1988). Chlorophyll a specific absorption and fluorescence excitation spectra for light-limited phytoplankton. *Deep Sea Research*, *35*(5), 639–663.

Monahan, A. H. (2012). The temporal autocorrelation structure of sea surface winds. *Journal of Climate*, *25*(19), 6684–6700.

Moum, J. N., & Smyth, W. D. (2001). Upper ocean mixing processes. In J. H. Steele, S. A. Thorpe, & K. K. Turekian, (Eds.), *Encyclopedia of Ocean Sciences* (Vol. 6, pp. 3093–3100). San Diego, CA: Elsevier.

Nelson, D. M., & Smith, W. O. J. (1986). Phytoplankton bloom dynamics of the western Ross Sea ice edge—II. Mesoscale cycling of nitrogen and silicon. *Deep Sea Research*, *33*, 1389–1412.

Orsi, A., Whitworth, T., & Nowlin, W. (1995). On the meridional extent and fronts of the Antarctic Circumpolar Current. *Deep Sea Research*, *42*(5), 641–673.

Owens, N. J. P., Priddle, J., & Whitehouse, M. (1991). Variations in phytoplanktonic nitrogen assimilation around South Georgia and in the Bransfield Strait (Southern Ocean). *Marine Chemistry*, *35*(1-4), 287–304.

Pearre, S. (2003). Eat and run? The hunger/satiation hypothesis in vertical migration: history, evidence and consequences. *Biological Reviews*, *78*(1), 1–79.

Perry, M. J., Sackmann, B. S., Eriksen, C. C., & Lee, C. M. (2008). Seaglider observations of blooms and subsurface chlorophyll maxima off the Washington coast. *Limnology and Oceanography*, *53*, 2169–2179.

Platt, T. (1972). Local phytoplankton abundance and turbulence. *Deep Sea Research*, *19*(3), 183–187.

Post, A. F., Dubinsky, Z., Wyman, K., & Falkowski, P. G. (1984). Kinetics of light-intensity adaptation in a marine planktonic diatom. *Marine Biology*, *83*, 231–238.

Powell, J. R., & Ohman, M. D. (2015). Covariability of zooplankton gradients with glider-detected density fronts in the Southern California Current System. *Deep Sea Research Part*, *II*(112), 79–90.

Prairie, J. C., Franks, P. J. S., Jaffe, J. S., Doubell, M. J., & Yamazaki, H. (2011). Physical and biological controls of vertical gradients in phytoplankton. *Limnology & Oceanography: Fluids & Environments*, *1*(1), 75–90.

Press, W. H., Teukolsky, S. A., Vetterling, W. T., & Flannery, B. P. (2007). *Numerical Recipes–The Art of Scientific Computing* (3rd ed., 773 pp.) Cambridge U.K: Cambridge University Press.

Priddle, J., Whitehouse, M., Atkinson, A., Brierley, A. S., & Murphy, E. J. (1997). Diurnal changes in near-surface ammonium concentration—interplay between zooplankton and phytoplankton. *Journal of Plankton Research*, *19*, 1305–1330.

Proctor, C. W., & Roesler, C. S. (2010). New insights on obtaining phytoplankton concentration and composition from in situ multispectral Chlorophyll fluorescence. *Limnology and Oceanography: Methods*, *8*, 695–708.

Read, J., Pollard, R., & Allen, J. (2007). Sub-mesoscale structure and the development of an eddy in the Subantarctic Front north of the Crozet Islands. *Deep Sea Research Part II: Topical Studies in Oceanography*, *54*(18-20), 1930–1948.

Reay, D., Priddle, J., Nedwell, D., Whitehouse, M., Ellis-Evans, J., Deubert, C., et al. (2001). Regulation by low temperature of phytoplankton growth and nutrient uptake in the Southern Ocean. *Marine Ecology Progress Series*, *219*, 51–64.

Resplandy, L., Boutin, J., & Merlivat, L. (2014). Observed small spatial scale and seasonal variability of the CO_2 system in the Southern Ocean. *Biogeosciences*, *11*(1), 75–90.

Resplandy, L., Levy, M., d'Ovidio, F., & Merlivat, L. (2009). Impact of submesoscale variability in estimating the air-sea CO_2 exchange: Results from a model study of the POMME experiment. *Global Biogeochemical Cycles*, *23*, GB1017. https://doi.org/10.1029/2008GB003239

Roesler, C., Uitz, J., Claustre, H., Boss, E., Xing, X., Organelli, E., et al. (2017). Recommendations for obtaining unbiased chlorophyll estimates from in situ chlorophyll fluorometers: A global analysis of WET Labs ECO sensors. *Limnology and Oceanography: Methods*, *15*(6), 572–585.

Rohr, T., Long, M. C., Kavanaugh, M. T., Lindsay, K., & Doney, S. C. (2017). Variability in the mechanisms controlling Southern Ocean phytoplankton bloom phenology in an ocean model and satellite observations. *Global Biogeochemical Cycles*, *31*, 922–940. https://doi.org/10.1002/2016GB005615

Roquet, F., Charrassin, J.-B., Marchand, S., Boehme, L., Fedak, M., Reverdin, G., et al. (2011). Delayed-mode calibration of hydrographic data obtained from animal-borne satellite relay data loggers. *Journal of Atmospheric and Oceanic Technology*, *28*(6), 787–801.

Roquet, F., Wunsch, C., Forget, G., Heimbach, P., Guinet, C., Reverdin, G., et al. (2013). Estimates of the Southern Ocean general circulation improved by animal-borne instruments. *Geophysical Research Letters*, *40*, 6176–6180. https://doi.org/10.1002/2013GL058304

Rosso, I., Hogg, A. M., Matear, R., & Strutton, P. G. (2016). Quantifying the influence of sub-mesoscale dynamics on the supply of iron to Southern Ocean phytoplankton blooms. *Deep-Sea Research Part*, *I*(115), 199–209.

Rumyantseva, A., Lucas, N., Rippeth, T., Martin, A., Painter, S. C., Boyd, T. J., & Henson, S. (2015). Ocean nutrient pathways associated with the passage of a storm. *Global Biogeochemical Cycles*, *29*, 1179–1189. https://doi.org/10.1002/2015GB005097

Russell, J., Sarmiento, J., Cullen, H., Hotinski, R., Johnson, K., Riser, S., et al. (2014). The Southern Ocean Carbon and ClimateObservations and Modeling Program (SOCCOM). *Ocean Carbon and Biogeochemistry News*, *7*, 1–28.

Ryther, J. H., & Hulburt, E. M. (1960). On winter mixing and the vertical distribution of phytoplankton. *Limnology and Oceanography*, *5*, 337–338.

Sackmann, B. S., Perry, M. J., & Eriksen, C. C. (2008). Seaglider observations of variability in daytime fluorescence quenching of chlorophyll-a in Northeastern Pacific coastal waters. *Biogeosciences Discussions*, *5*, 2839–2865. https://doi.org/10.5194/bgd-5-2839-2008

Sakshaug, E., & Holm-Hansen, O. (1986). Photoadaptation in Antarctic phytoplankton: Variations in growth rate, chemical composition and P versus I curves. *Journal of Plankton Research*, *8*(3), 459–473.

Sallée, J.-B., Wienders, N., Speer, K., & Morrow, R. (2006). Formation of subantarctic mode water in the southeastern Indian Ocean. *Ocean Dynamics*, *56*(5-6), 525–542.

Sanford, T. B., Dunlap, J. H., Carlson, J. A., Webb, D. C., & Girton, J. B. (2005). Autonomous velocity and density profiler: EM-APEX. In *Proceedings of the IEEE/OES Eighth Working Conference on Current Measurement Technology* (pp. 152–156).

Sharoni, S., Ovidio, F. d. r., Vardi, A., Boss, E., Lehahn, Y., & Koren, I. (2017). Dispersion/dilution enhances phytoplankton blooms in low-nutrient waters. *Nature Communications*, *8*(14868). https://doi.org/10.1038/ncomms14868

Siegel, D. A., Maritorena, S., Nelson, N. B., Hansell, D. A., & Lorenzi-Kayser, M. (2002). Global distribution and dynamics of colored dissolved and detrital organic materials. *Journal of Geophysical Research*, *107*(C12), 3228. https://doi.org/10.1029/2001JC000965

Simmonds, I., & Keay, K. (2000). Mean Southern Hemisphere extratropical cyclone behavior in the 40-year NCEP-NCAR Reanalysis. *Journal of Climate*, *13*(5), 873–885.

Simmonds, I., Keay, K., & Lim, E.-P. (2003). Synoptic activity in the seas around Antarctica. *Monthly Weather Review*, *131*, 272–288.

Smetacek, V., Klaas, C., Strass, V. H., Assmy, P., Montresor, M., Cisewski, B., et al. (2012). Deep carbon export from a Southern Ocean iron-fertilized diatom bloom. *Nature*, *487*(7407), 313–319.

Smith, W. O. J., Nelson, D. M., & Mathot, S. (1999). Phytoplankton growth rates in the Ross Sea, Antarctica, determined by independent methods: Temporal variations. *Journal of Plankton Research*, *21*, 1519–1536.

Spies, A. (1987). Growth rates of Antarctic marine phytoplankton in the Weddell Sea. *Marine Ecology Progress Series*, *41*, 267–274.

Stramska, M., & Dickey, T. D. (1992). Variability of bio-optical properties of the upper ocean associated with diel cycles in phytoplankton population. *Journal of Geophysical Research*, *97*(C), 17,873–17,887.

Strutton, P. G., Mitchell, J. G., & Parslow, J. (1997). Phytoplankton patchiness: Quantifying the biological contribution using Fast Repetition Rate Fluorometry. *Journal of Plankton Research*, *19*(9), 1265–1274.

Sullivan, J. M., & Twardowski, M. S. (2009). Angular shape of the oceanic particulate volume scattering function in the backward direction. *Applied Optics*, *48*, 6811–6819.

Swart, S., Thomalla, S. J., & Monteiro, P. M. S. (2015). The seasonal cycle of mixed layer dynamics and phytoplankton biomass in the Sub-Antarctic Zone: A high-resolution glider experiment. *Journal of Marine Systems*, *147*(C), 103–115.

Talley, L. D., Pickard, G. L., Emery, W. J., & Swift, J. H. (2011). Chapter 4 - typical distributions of water characteristics. In L. D. Talley, G. L. Pickard, W. J. Emery, & J. H. Swift (Eds.), *Descriptive Physical Oceanography* (6th ed., pp. 67–110). Boston, MA: Academic Press. https://doi.org/10.1016/B978-0-7506-4552-2.10004-6

Taylor, J. R. (2016). Turbulent mixing, restratification, and phytoplankton growth at a submesoscale eddy. *Geophysical Research Letters*, *43*, 5784–5792. https://doi.org/10.1002/2016GL069106

Taylor, J. R., & Ferrari, R. (2011a). Shutdown of turbulent convection as a new criterion for the onset of spring phytoplankton blooms. *Limnology and Oceanography*, *56*, 2293–2307.

Taylor, J. R., & Ferrari, R. (2011b). Ocean fronts trigger high latitude phytoplankton blooms. *Geophysical Research Letters*, *38*, L23601. https://doi.org/10.1029/2011GL049312

Taylor, A. G., Goericke, R., Landry, M. R., Selph, K., Wick, D. A., & Roadman, M. J. (2012). Sharp gradients in phytoplankton community structure across a frontal zone in the California Current Ecosystem. *Journal of Plankton Research*, *34*(9), 778–789.

Therriault, J.-C., Booth, D. A., Legendre, L., & Demers, S. (1990). Phytoplankton photoadaptation to vertical excursion as estimated by an in vivo fluorescence ratio. *Marine Ecology Progress Series*, *60*, 97–111.

Therriault, J.-C., Lawrence, D. J., & Platt, T. (1978). Spatial variability of phytoplankton turnover in relation to physical processes in a coastal environment. *Limnology and Oceanography*, *23*, 900–911.

Therriault, J.-C., & Platt, T. (1978). Spatial heterogeneity of phytoplankton biomass and related factors in the near-surface waters of an exposed coastal embayment. *Limnology and Oceanography*, *23*, 888–899.

Thompson, A. F., Lazar, A., Buckingham, C., Naveira Garabato, A. C., Damerell, G. M., & Heywood, K. J. (2016). Open-ocean submesSoscale motions: A full seasonal cycle of mixed layer instabilities from gliders. *Journal of Physical Oceanography*, *46*(4), 1285–1307.

Thorpe, S. A. (1977). Turbulence and mixing in a Scottish Loch. *Philosophical Transactions of the Royal Society of London. Series A Mathematical and Physical Sciences*, *286*, 125–181.

Thorpe, S. A. (2007). Turbulence in oceanic boundary layers. In *An introduction to ocean turbulence* (pp. 77–115). Cambridge: Cambridge University Press. https://doi.org/10.1017/CBO9780511801198.007

Timmermans, K. R., Gerringa, L. J. A., de Baar, H. J. W., van der Wagt, B., Veldhuis, M. J. W., de Jong, J. T. M., et al. (2001). Growth rates of large and small Southern Ocean diatoms in relation to availability of iron in natural seawater. *Limnology and Oceanography*, *46*(2), 260–266.

Timmermans, K. R., van der Wagt, B., & De Baar, H. J. W. (2004). Growth Rates, Half-Saturation Constants, and Silicate, Nitrate, and Phosphate Depletion in Relation to Iron Availability of Four Large, Open-Ocean Diatoms from the Southern Ocean. *Limnology and Oceanography*, *49*(6), 2141–2151.

Tzella, A., & Haynes, P. H. (2007). Small-scale spatial structure in plankton distributions. *Biogeosciences*, *4*(2), 173–179.

Ulbrich, U., Leckebusch, G. C., & Pinto, J. G. (2009). Extra-tropical cyclones in the present and future climate: A review. *Theoretical and Applied Climatology*, *96*(1-2), 117–131.

Vera, C. (2003). Interannual and interdecadal variability of atmospheric synoptic-scale activity in the Southern Hemisphere. *Journal of Geophysical Research*, *108*(C4), 8077. https://doi.org/10.1029/2000JC000406

Viglione, G. A., Thompson, A. F., Flexas, M. M., Sprintall, J., & Swart, S. (2018). Abrupt transitions in submesoscale structure in Southern Drake Passage: Glider observations and model results. *Journal of Physical Oceanography*, *48*, 2011–2027. https://doi.org/10.1175/JPO-D-17-0192.1

Westberry, T., Behrenfeld, M., Siegel, D. A., & Boss, E. (2008). Carbon-based primary productivity modeling with vertically resolved photoacclimation. *Global Biogeochemical Cycles*, *22*, GB2024. https://doi.org/0.1029/2007GB003078

Whitt, D. B., Lévy, M., & Taylor, J. R. (2017). Low-frequency and high-frequency oscillatory winds synergistically enhance nutrient entrainment and phytoplankton at fronts. *Journal of Geophysical Research: Oceans*, *122*, 1016–1041. https://doi.org/10.1002/2016JC012400

Whitt, D. B., & Taylor, J. R. (2017). Energetic Submesoscales Maintain Strong Mixed Layer Stratification during an Autumn Storm. *Journal of Physical Oceanography*, *47*(10), 2419–2427.

Whitt, D. B., Taylor, J. R., & Levy, M. (2017). Synoptic-to-planetary scale wind variability enhances phytoplankton biomass at ocean fronts. *Journal of Geophysical Research: Oceans*, *122*, 4602–4633. https://doi.org/10.1002/2016JC011899

Xing, X., Claustre, H., Blain, S., D'ortenzio, F., Antoine, D., Ras, J., et al. (2012). Quenching correction for in vivo chlorophyll fluorescence acquired by autonomous platforms: A case study with instrumented elephant seals in the Kerguelen region (Southern Ocean). *Limnology and Oceanography: Methods*, *10*, 483–495.

Xing, X., Claustre, H., Boss, E., Roesler, C., Organelli, E., Poteau, A., et al. (2016). Correction of profiles of in-situ chlorophyll fluorometry for the contribution of fluorescence originating from non-algal matter. *Limnology and Oceanography: Methods*, *15*(1), 80–93.

Zawada, D. G., Zaneveld, J. R. V., Boss, E., Gardner, W. D., Richardson, M. J., & Mishonov, A. V. (2005). A comparison of hydrographically and optically derived mixed layer depths. *Journal of Geophysical Research*, *110*, C11001. https://doi.org/10.1029/2004JC002417

Zhang, X., Hu, L., & He, M.-X. (2009). Scattering by pure seawater: Effect of salinity. *Optics Express*, *17*(7), 5698–5710.